

xFLIE: Leveraging Actionable Hierarchical Scene Representations for Autonomous Semantic-Aware Inspection Missions

Vignesh Kottayam Viswanathan, Mario A.V. Saucedo, Sumeet Gajanan Satpute, Christoforos Kanellakis and George Nikolakopoulos

arXiv:2412.19571v1 [cs.RO] 27 Dec 2024

Abstract—This article presents *xFLIE*, a fully integrated 3D hierarchical scene graph based autonomous inspection architecture. Specifically, we present a tightly-coupled solution of incremental 3D *Layered Semantic Graphs* (LSG) construction and real-time exploitation by a multi-modal autonomy, *First-Look based Inspection and Exploration* (FLIE) planner, to address the task of inspection of apriori unknown semantic targets of interest in unknown environments. This work aims to address the challenge of maintaining, in addition to or as an alternative to volumetric models, an intuitive scene representation during large-scale inspection missions. Through its contributions, the proposed architecture aims to provide a high-level multi-tiered abstract environment representation whilst simultaneously maintaining a tractable foundation for rapid and informed decision-making capable of enhancing inspection planning through scene understanding, *what should it inspect ?*, and reasoning, *why should it inspect ?*. The proposed LSG framework is designed to leverage the concept of *nesting* lower local graphs, at multiple layers of abstraction, with the abstract concepts grounded on the functionality of the integrated FLIE planner. Through intuitive scene representation, the proposed architecture offers an easily digestible environment model for human operators which helps to improve situational awareness and their understanding of the operating environment. We highlight the use-case benefits of hierarchical and semantic path-planning capability over LSG to address queries, by the integrated planner as well as the human operator. The validity of the proposed architecture is evaluated in large-scale simulated outdoor urban scenarios as well as being deployed onboard a Boston Dynamics Spot quadruped robot for extensive outdoor field experiments.

Index Terms—Autonomous agents, Inspection planning, Semantic scene understanding, Scene graphs

I. INTRODUCTION

THE introduction of constructing and maintaining a hierarchical scene representation has generated tremendous interest for pursuing novel applications in recent years [1]. The transition from traditional metric environment models to an abstracted multi-resolution hierarchical scene representation has enabled robotic platforms to interpret a rich and expressive model of their operating environment. A common methodology to structure the hierarchical scene model is to ground the semantic concepts as nodes in a graph, with nodes clustered at various layers based on the level of detail they capture [2]–[4]. For example, recent works leverage such scene graphs

to address tasks such as robot manipulation [5]–[7], task planning [8], [9], simultaneous localization and mapping [4], [10], [11], semantic navigation [12]–[14], autonomous operations [15] and embodied intelligence [16], [17].

Hierarchical scene graphs offer significant advantages for data manipulation and task-specific processing in long-term autonomous missions by allowing selective access to relevant subsets of information. This capability reduces the computational load by enabling the autonomy system to focus only on the most pertinent data, depending on the task at hand. Furthermore, the intrinsic flexibility in manipulating specific sub-graphs, offered by the hierarchical nature, enhances an autonomy’s ability to adapt to different phases of the mission, supporting efficient planning, informed decision-making, and improving overall situational awareness of the robot during a mission.

The scope of this work focuses on integrating such scene graph representation with a multi-modal planning autonomy for inspection of apriori unknown targets-of-interest in an unknown environment. Existing inspection frameworks primarily focus on reconstructing a 3D representation of the environment [18]–[20], within the limited lifetime of the mission, based on planning over volumetric model of the environment. While being a highly relevant approach when considering the task of reconstruction, such frameworks fall short when a contextual inspection mission is considered, such as Urban Search and Rescue (USAR) operations. In such scenarios, the constructed 3D model requires further post-processing by operators to identify potential characteristics or regions of interest that may require further detailed investigation. This would take time and effort which may be in limited availability. Thus, in this work, we address the need to maintain an intuitive understanding of the environment during an inspection mission that can be leveraged by both the onboard autonomy as well as by human operators. Overall, our goal is to enhance the performance of the onboard autonomy through integration with an incrementally constructed 3D hierarchical scene graph that structures an operating environment based on abstract semantic concepts relevant to the context of an inspection mission. Figure. 1 presents a visualization of the hierarchical scene graph constructed and leveraged for a simulated use-case of autonomous inspection of apriori unknown targets-of-inspection in an unknown urban city environment. The autonomy was instructed to inspect $\{car, truck\}$ semantics.

The authors are with Robotics and AI, Luleå University of Technology 97187, Luleå, Sweden

Corresponding author: Vignesh Kottayam Viswanathan (email: vigkot@ltu.se).

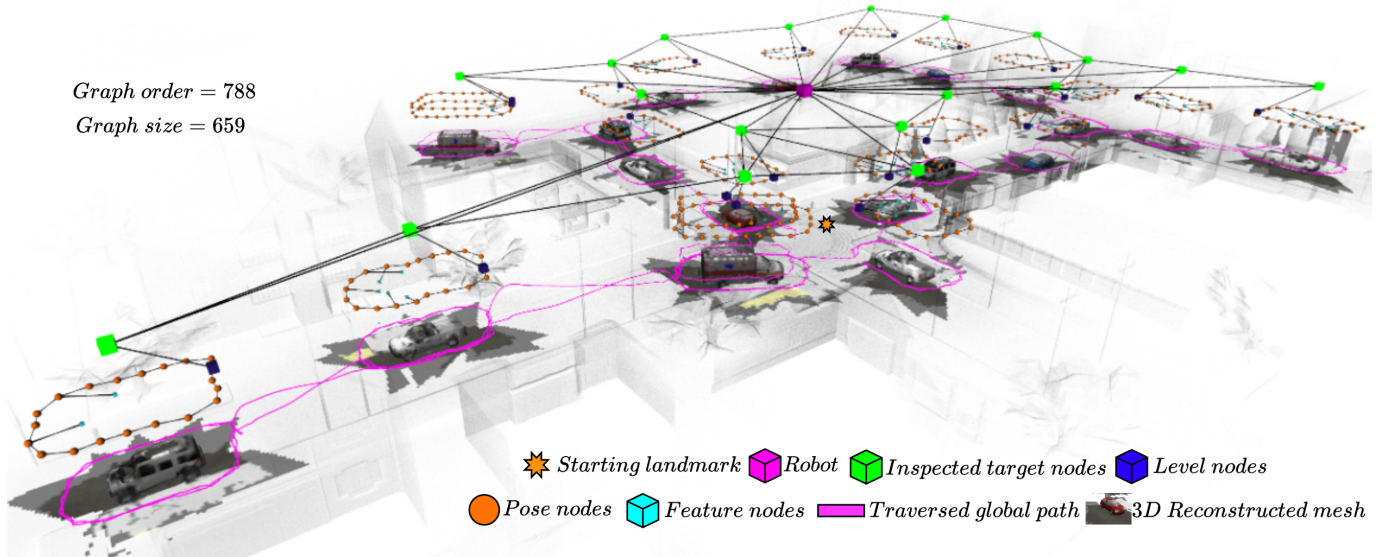


Fig. 1. We present *xFLIE*, a multi-modal planning autonomy framework designed for constructing and exploiting characteristic 3D hierarchical Layered Semantic Graphs (LSG) of previously unknown targets in uncharted environments. The accompanying figure illustrates a 3D LSG constructed during a simulated inspection mission in an urban city environment. Leveraging this semantic scene representation, we demonstrate the framework’s ability to empower human operators to efficiently interpret the scene and deploy extended inspection missions by addressing semantic queries over the 3D LSG.

II. RELATED WORKS

Hierarchical scene representation of unknown environments: [21] presents the foundation principles of representing the perceived environment in the form of an internal spatial-semantic hierarchy for a robot. In their work, the authors bifurcate the perceived knowledge into a hierarchical representation capturing metric information and one hierarchy representing the symbolic abstract concepts. To address and complete high-level semantic queries (such as *go to the bedroom*), the authors correlate the two representation with the concept of “anchoring” the corresponding nodes in the hierarchies. Thus, grounding the abstract concept of a *bedroom* to a spatial node containing the 3D information from onboard perception modules. [22] investigates a multi-layered metric-semantic approach to represent abstract concepts of the perceived environment. In their work, the authors address the goal of reasoning over the layered representation by augmenting the layers of the hierarchical graph with spatial, topological and conceptual information. More recently, [3] presents a layered 3D scene graph structure based on input 3D mesh and RGB information. Addressing the task of generating scene graph of indoor environments, the authors cluster nodes based semantic concepts (e.g., *buildings, rooms, objects*) in various layers. The work by [10] investigates the generation of 3D dynamic scene graphs based on stereo optical sensor providing point-cloud and image information for Simultaneous Localization and Mapping (SLAM) tasks. Building the 3D scene graph *bottom-up* from low-level parametric information, semantic concepts are then segmented from the 3D mesh and the nodes clustered into corresponding abstraction layers. Extending the work in [10] to real-time graph construction, [4] presents an incremental 3D scene graph generation framework to produce a rich metric-semantic map of the environment. [23] presents a multi-layered hierarchical model

for navigating in indoor environments. In their work, the authors consider an input visibility graph which is then later processed to extract geometric elements in deeper levels using graph partitioning algorithms. [13] introduces a hierarchical representation considering topological, semantic and spatial concepts aimed towards improving robust localization and mapping techniques in indoor environments. By processing onboard LiDAR information, the authors follow a *bottom-up* process of graph generation, with the lowest layer containing localization information and the highest layer encompassing the semantic concepts (e.g. *corridors, rooms*). The intermediate layer consists of segmented mesh from the locally observed point-cloud representation of the environment.

Inspection in unknown environments: Inspection planning in an unknown environment is well-addressed problem with current approaches balancing exploration with coverage planning. Largely, information theoretic sampling-based strategies have deployed a variation of Next-Best-View (NBV) planning. These approaches address the objective to identify the optimal camera viewpoint configuration that maximizes information gathered, reduces energy expenditure, and achieves the desired level of reconstruction accuracy based on a 3D representation of the environment [18], [24]–[26]. At the exploration and inspection planning stage, previously mentioned studies aim to achieve complete coverage of the environment by systematically exploring all unknown regions. [27] addresses the task of inspection of distributed structures in an unknown environment through a reactive map-free inspect-explore approach. In [28], the authors demonstrate a Rapidly-growing Random Tree (RRT) based targeted exploration and mapping scheme by considering, in addition to conventional volumetric gain formulation, a heuristic that quantifies the likelihood of a voxel belonging to a specific semantic class. [19] introduces a frontier-based volumetric-exploration approach integrated

with semantics-aware coverage path-planning for inspecting semantics-of-interest in unknown environments. [29] presents a belief-behaviour graph based inspection planning of semantics of interest in unknown urban environments. In their work, the authors present an approach that considers the uncertainty in observations and semantic understanding of the environment to help execute the optimal semantic behaviour which can complete the inspection of a semantic object.

A. Contributions

The proposed novel work aims for the first ever time to unite the field of semantic scene structuring with that of inspection planning of apriori unknown targets-of-interest in unknown environments. An audio-visual media presenting the proposed architecture can be accessed here: <https://youtu.be/kJgDqer7I3Y>. We achieve this through a tightly-coupled solution that constructs and exploits, in real-time, 3D scene graphs by an integrated multi-modal inspection-exploration planner to survey the environment and inspect relevant semantic targets-of-interest.

Specifically, compared with conventional inspection planning approaches [18], [24]–[26], that construct and provide an *as-is* volumetric environment model at the end of the mission, our framework constructs and maintains an intuitive environment model by representing semantic concepts in various layers of abstraction. This forms as our first contribution C1: establishing a novel foundational solution of incremental and real-time construction of a planner-centric actionable hierarchical scene graph (in Section. III): **3D Layered Semantic Graphs** (LSG). *LSG* is a *layered* and *nested* graph built *top-down* to register and maintain characteristic actionable knowledge of an apriori unknown inspection target during the lifetime of the inspect-explore autonomy. *LSG* is *layered* and *nested*, such that the graphs at every layer are populated based on the abstraction representing different types of information provided by the planner. The *nested* concept is realized through assigning graphs at deeper layers as attributes of the parent nodes in the layer above. The nodes within each graph model semantic concepts with intra-layer edges, capturing spatial or symbolic relationships. The graph is *actionable*, as the constituent nodes, edges and its encoded attributes can be leveraged by the mission planner to address runtime objectives during the mission.

Moreover, by leveraging a semantic scene model, we augment the onboard autonomy with the capability of scene understanding, i.e. *what it should inspect*?, and reasoning, i.e. *why it should inspect it*?. Specifically, our approach constructs a *characteristic* semantic scene graph *top-down* of an inspected target rather than *estimating* the 3D scene graph *bottom-up* of an environment from corresponding sensor measurements [4], [10], [13]. Additionally, we differentiate the proposed graph construction framework from the existing inspection-related works by leveraging the constructed 3D scene model for addressing real-time queries pertaining to both inspection and path-planning by the integrated multi-modal autonomy. For human operators, the shared intuitive scene representation reduces the time needed to process and interpret

collected information, offering an accessible and efficient way to understand the operating environment. This forms our second contribution C2: **xFLIE: Enhanced First-Look Inspect-Explore Autonomy**, the first-of-its kind multi-modal planning autonomy that aims to construct and exploit 3D hierarchical scene representation for semantics-aware inspection in unknown environments (refer Sec. V). xFLIE is a modular autonomy comprising of FLIE [27]: An *inspection* planner, an *exploration* planner, and the 3D *LSG* constructor working in tandem to address mission objectives. It leverages the map-free reactive planning provided by the FLIE autonomy and exploits the high-level semantic abstractions within LSG to make an informed decision to inspect a semantic of interest. We *enhance* the robot autonomy with the scene understanding and reasoning ability, achieved through leveraging the 3D LSG for mission planning. Additionally, we highlight the advantages of online **hierarchical** and **semantic path-planning** capability over LSG to address inspection planning, as well as operator queries (in Sec. V-C).

Furthermore, we evaluate the performance of the proposed approach in large-scale environments with an increasing number of inspection targets. Since the LSG is incrementally constructed for each inspected semantic target, its overall attributes—such as graph size and order—grow proportionally, which can impact the efficiency of planning over large graphs. This leads to our third contribution, C3: analyzing the scalability and performance of 3D LSG hierarchical representation for planning in expansive environments. To highlight the benefits of the proposed method, we compare its performance against traditional volumetric maps for waypoint navigation tasks during inspection (refer to Sec. VII-C).

Finally, the fourth contribution, C4, presents rigorous validation of the proposed framework in a large-scale simulated urban environment on an aerial platform (refer to Sec. VII-A), complemented by extensive field experiments using the Boston Dynamics Spot quadrupedal robotic platform (refer to Sec. VII-B).

In comparison to its previous development of FLIE [27], the current implementation introduces notable improvements, particularly through its integration with the 3D LSG. Firstly, the earlier inspection planner was agnostic to the context of semantic targets of interest, leading to a comprehensive inspection of all objects in the operating environment. In contrast, the current work incorporates real-time scene understanding through semantic target detection and localization, enabling a focused inspection of specific elements of interest in semantically rich environments. Secondly, the prior approach relied on a naive inspection target evaluation method, which based decisions solely on the size of geometric information (e.g., 3D point clouds) registered during exploration. Our current implementation advances the decision-making skill by integrating a weighted gain formulation leveraging the 3D LSG. This formulation factors in key functional considerations, such as the target’s proximity to the robot, its relevance for inspection, and its proximity to other inspection targets (refer to Sec. V-A).

III. 3D LAYERED SEMANTIC GRAPH

This section describes the methodology behind the top-down construction of layers prescribed within the 3D hierarchical graph during autonomous inspection missions. Figure. 2 presents a runtime visual highlighting the incremental construction of 3D LSG during an inspect-explore mission.

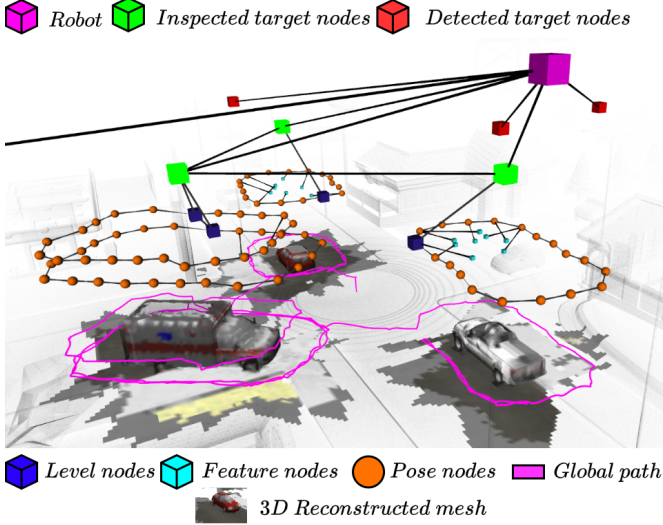


Fig. 2. A graphical overview on the construction of 3D Layered Semantic Graphs during autonomous inspection of $\{car, truck\}$ semantics in the urban city Gazebo world. The 3D reconstruction is undertaken by Nvblox [30] and is presented for visualization purposes.

A. Preliminaries

In this work, we construct a top-down hierarchical 3D graph composed of multiple abstraction layers. The consideration provided to the abstractions are such that they are defined based on the resolution of information they encode during the inspect-explore mission. To that extent, we denote $\mathbb{L} = [Target, Level, Pose, Feature]$, as the set of abstraction layers that constitute the 3D hierarchical graph. Let $\mathcal{G}_l = (\mathcal{V}_l, \mathcal{E}_l, \mathcal{A}_l)$ be an undirected graph of layer $l \in \mathbb{L}$ with an ordered set of nodes \mathcal{V}_l and edges \mathcal{E}_l . Let $a_l \in \mathcal{A}_l$ be the attribute of a node $v_l \in \mathcal{V}_l$ encoded with necessary metric, sensor and semantic information for planning, in addition to the graph of the next layer. We denote the set of semantic elements \mathcal{S} , desired to be segmented during exploration $s_e \in \mathcal{S}$ and inspection $s_i \in \mathcal{S}$.

In this research, we move away from maintaining a global subgraph representation for every abstraction layer compared to state-of-art works [4], [10], [13]. Instead, we consider graphs of deeper layers populated during inspection, i.e. *Level*, *Pose* and *Feature* layers as characteristic local knowledge of the parent node contained within the graph of upper layer. Specifically, each abstraction layer contains multiple unique and local instances of the corresponding graph encoded to every parent node in the layer above. For example, considering the *Level* layer, every inspected semantic target node would nest and maintain a unique and local representation of the graph containing the level nodes registered during inspection of that semantic target. Thus, the *Level* layer would instead

constitute a collection of such local graphs rather than a monolithic subgraph representing all the level nodes registered for all targets inspected.

The proposed LSG excludes the typical consideration of inter-layer edges during construction and subsequently for path-planning. Instead, we introduce the concept of a *layer frontier node* $v_l^H \subseteq \mathcal{V}_l \in \mathcal{G}_l$, which enables the planner to transcend between isolated local graphs in different layers by expanding the encoded attributes of the respective node. A *layer frontier node* functions as both a child in its local graph and a parent in the nested graph, enabling the planner to exploit the latent property of nested graphs during hierarchical planning. This means that local graphs remain hidden from the planner until required, enabling the planner to access and expand them, as and when needed, when navigating across layers.

While v_l^H enables transition between different local layers, i.e. layer-to-layer, we introduce the concept of a *bridge node* that functions to specifically enable transition between the node representations, i.e. node-to-node, in the highest abstraction layer graph, i.e. *Target* layer graph. Since the nodes themselves are a symbolic representation of inspected targets, the intra-layer connections represent abstract spatially-weighted relation and not an actual path that can be tracked by the robot. For example, to move from *Building-A* to *Building-B*, the general logic applied by humans is to navigate towards the *lobby* floor of *Building-A*, cross a *street* or a *corridor* to reach the *entrance* or *lobby* floor of *Building-B*. At this point, it is considered that *Building-B* has been reached. In this work, we implement an analogous approach, where the task at the highest-level is broken down into a set of low-level navigation points, $v_L^B \subseteq \mathcal{V}_L$ and $v_P^B \subseteq \mathcal{V}_P \setminus \mathcal{G}_P = a_L(v_L^B)$, within LSG that can be tracked by the robot. These navigation points are referred to as *bridge nodes* in this work, reaching which enables the planner to transition between the nodes in \mathcal{G}_T .

Additionally, we subscribe to the following notations where the operator $\|\cdot\|$ denotes the Euclidean norm and the operator $|\cdot|$ denotes the cardinality of a set, which refers to the number of elements in the respective set.

Terminologies: We distinguish between the terms, *semantic targets* and *semantic features*, as follows: (a) *semantic targets* refer to targets of interest, such as *car*, *house*, or *truck*, that is observed in the environment as candidates for further inspection; and (b) *semantic features* refer to the observed and segmented features of a semantic target, such as the *window* or *door* of a house, or the *hood* of a car.

B. Layers Construction

Target Layer: During exploration of the environment, detected semantic targets are registered as nodes within the graph \mathcal{G}_T representing this layer. The child nodes within this graph can be differentiated into two main subsets, $\{v_T^I\}, \{v_T^D\} \subseteq \mathcal{V}_T$, where $v^I \in \{v_T^I\}$ denotes the set of target nodes that have been inspected and $v^D \in \{v_T^D\}$ denoting the set of nodes that have been detected and are remaining to be inspected.

During registration of nodes while exploring, the nodes are encoded with the following attribute $a_T \in \mathcal{A}_T$: (i) estimated

3D location of the target $\hat{\mathbf{X}}_{target} \in \mathbb{R}^3$, (ii) visual RGB image information of the registered target, (iii) the semantic class of the detected target s_e , (iv) the confidence of the semantic $s_e^c \in \mathbb{R}^+$, (v) the segmented area of semantic $s_e^a \in \mathbb{R}^+$, and (vi) a utility heuristic $U \in \mathbb{R}^+$ quantifying the relevance for inspection of the detected semantic node.

Once a v^D node undergoes inspection, the attributes of the node is subsequently augmented with the graph representation of the nested *Level* layer and its corresponding *Pose* and *Feature* layer graphs. Additionally, a convex polygon \mathbb{P} , constructed from the 2D spatial attributes of the child nodes within the *Pose* layer graph of the first level of inspection, is encoded to its attribute. Due to the framework's overall independence from environmental occupancy knowledge, polygon-based containment checking effectively prevents duplicate registration of targets. For more detailed information on the \mathbb{P} construction and its use, the readers are directed to Sec. V-B.

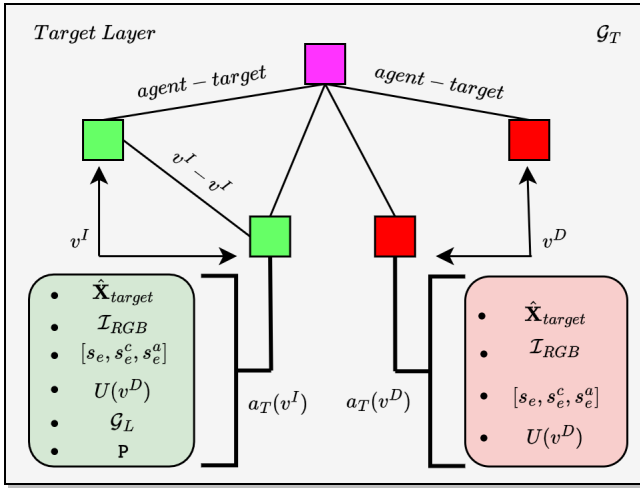


Fig. 3. A conceptual visualization of the internal composition of the *Target* layer graph (\mathcal{G}_T) within the 3D LSG.

Intra-layer connections occur between the registered target nodes and the parent node, as well as between v^I - v^I nodes. The parent node within the *Target* layer is modelled to be a representation of the robotic agent encoded with information on the current 6D pose of the robot $\mathbf{X}_{odom} \in \mathbb{R}^3 \times \mathbb{SO}(3)$. The edge existing between parent-child nodes is weighted with spatial information capturing the Euclidean distance between the two nodes. The edge connecting two v^I nodes is also weighted in similar manner but its existence is determined based on satisfying certain conditions.

Specifically, the edge connecting two v^I nodes is determined by a confluence of factors. Primarily, to ensure unobstructed region exists between the two nodes that share an edge, only valid subset of $\{v_T^{I,wsr}\} \subseteq \{v_T^I\}$ nodes that lie within sensor range $d_{max} \in \mathbb{R}^+$ and the visual field-of-view of the robot $\alpha \in \mathbb{R}^+$ are considered. That is, post inspection and during exploration around the current target node $v_T^{I,curr}$, an edge is shared between $v_T^{I,curr}$ and $\{v_T^{I,wsr}\}$ if nodes within $\{v_T^{I,wsr}\}$ are directly observable from $v_T^{I,curr}$ and whose estimated position lie inside the polygon representation (refer Sec. V-B). Figure. 3 presents a concept diagram of the internal

composition of \mathcal{G}_T within the *Target* layer of 3D LSG during its construction.

Level Layer: The *Level* layer graph \mathcal{G}_L of the target node under inspection comprises of child nodes $v_L \in V_L$, representing the various levels of inspection executed for the current target node, such as *Level-0*, *Level-1* and so on. In particular, either at the start of inspection of the target node or when the robot is commanded to the next level of inspection by the planner, the graph is populated with the node representation of the current level of inspection. The readers are directed to [27] for a detailed explanation of the logic behind the implemented policy directed towards establishing levels of inspection.

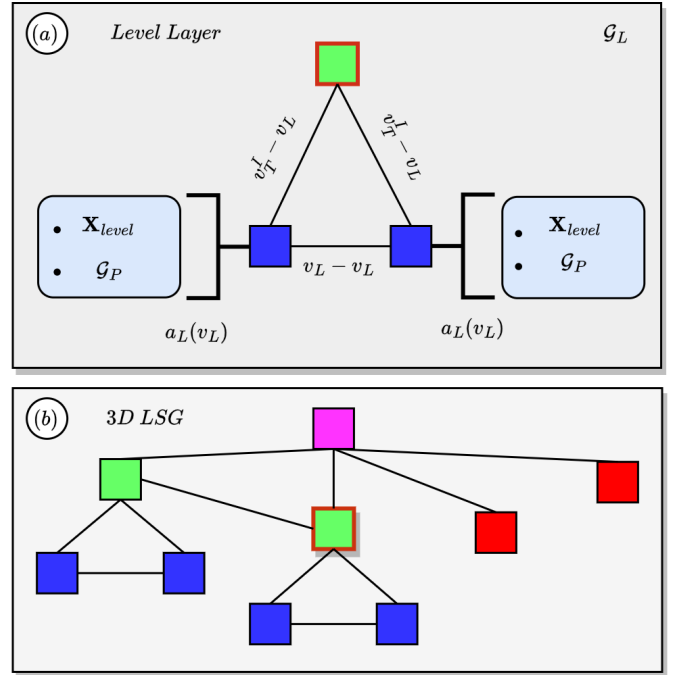


Fig. 4. A conceptual visualization of (a) the internal composition of the *Level* layer graph (\mathcal{G}_L) of the current target node being inspected (highlighted through red border). (b) presents an overall global structure of 3D LSG with the populated *Level* layer graph under the current inspection target.

The nodes within this layer are encoded with the following attribute $a_L \in A_L$: (i) 3D position of the node ($\mathbf{X}_{level} \in \mathbb{R}^3$), and (ii) the *Pose* layer graph containing the commanded view-poses at the current level of inspection. The current target node being inspected, serves as parent node within this graph. Symbolic intra-layer connections exist between the parent node and the child nodes, however, edges connecting adjacent v_L nodes are assigned weights corresponding to the Euclidean distance between their respective 3D spatial coordinates. Figure. 4(a) visualizes the composition of the *Level* layer graph alongside the registered attributes, populated during inspection of the current target node (highlighted through red border). In Fig. 4(b), the subsequent structure of the 3D LSG obtained after the combining \mathcal{G}_T and \mathcal{G}_L is presented.

Pose Layer: The *Pose* layer graph \mathcal{G}_P of the current inspection level comprises of child nodes representing the view-poses planned by the inspection policy. Each child node within this graph is encoded with the following attribute $a_P \in A_P$:

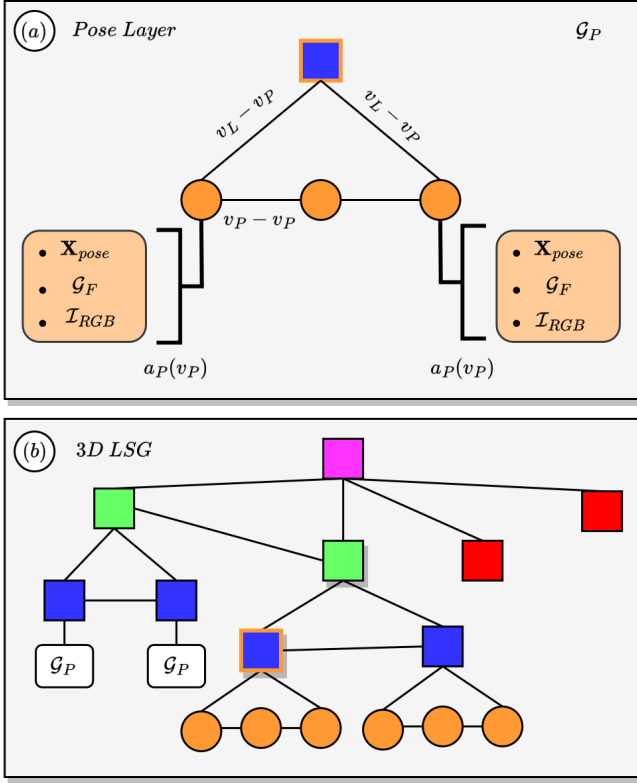


Fig. 5. A conceptual visualization of (a) the internal composition of the *Pose* layer graph (\mathcal{G}_P) of the current target node being inspected (highlighted through *orange* border). (b) presents an overall global structure of 3D LSG with the populated *Pose* layer graph under an inspection level node.

(i) 6D pose of the node ($\mathbf{X}_{pose} \in \mathbb{R}^3 \times SO(3)$), representing the commanded view-pose during inspection, (ii) visual RGB image information captured at the commanded view-pose, and (iii) the *Feature* layer graph containing observed semantic features from the current pose node. The current inspection level node serves as the parent node of \mathcal{G}_P , sharing an edge with initial and final pose nodes registered during inspection of the current level (highlighted through *orange* border). The edges are weighted with the Euclidean distance between their respective 3D spatial coordinates. Additionally, each pose node shares a weighted edge with its adjacent pose node. Figure 5(a) presents a graphical representation of the internal composition of \mathcal{G}_P , registered and populated under an inspection level node. Figure 5(b) visualizes the overall structure of 3D LSG, concatenated with the corresponding *Pose* layer graphs for each level of inspection.

Feature Layer: The *Feature* layer graph \mathcal{G}_F registers characteristic semantic features of the target node observed during inspection. Leveraging onboard segmentation, the semantics are extracted from the RGB image frame in real-time and localized in 3D space. The nodes are encoded with the following attributes $a_F \in A_F$: (i) 3D position $\hat{\mathbf{X}}_{feature} \in \mathbb{R}^3$, (ii) semantic class s_i , (iii) detected confidence $s_i^c \in \mathbb{R}^+$, and (iv) segmented area $s_i^a \in \mathbb{R}^+$. Each feature node shares a symbolic edge with the parent pose node from which it was observed. Figure. 6(a) visualizes the populated \mathcal{G}_F capturing the observed semantic features alongside their registered

characteristic attributes at the current inspection view-pose node (highlighted through *blue* border) during inspection. Figure. 6(b) presents the final structure of 3D LSG, with the relevant layers populated during inspection of a semantic target.

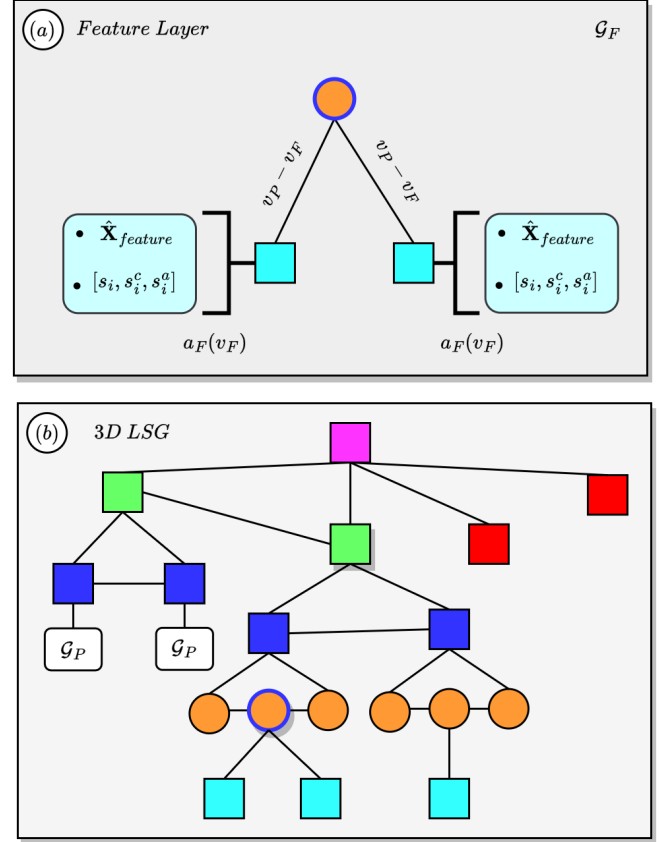


Fig. 6. A conceptual visualization of (a) the internal composition of the *Feature* layer graph (\mathcal{G}_F) of a visited inspection pose node (highlighted through *blue* border). (b) presents an overall global structure of 3D LSG with the populated *Feature* layer graph under an inspection pose node

Figure. 7 presents a runtime visualization capturing the internal composition of 3D LSG constructed during a simulated inspection mission. (On *top*), registration of observed semantic targets as nodes within \mathcal{G}_T during exploration is represented. (On *bottom-right*), the registered levels of inspection (*blue*-colored boxes) of an observed semantic target, highlighted within the *square-box*, is presented. A sample of the registered pose and feature layer nodes is shown in the *bottom-left*, as *orange* spheres and *cyan*-colored boxes respectively.

IV. SCENE PROCESSING: SEMANTIC SEGMENTATION AND LOCALIZATION

In this Section, we present in detail the technical aspects related to semantic segmentation and localization. The module is bifurcated into two main sections which address the following tasks: (a) Semantic Segmentation: segmentation of desired semantics, and (b) Semantic Localization: localization of the segmented semantics in 3D space. Figure. 8 presents the process pipeline of the implemented scene processing module in this work.

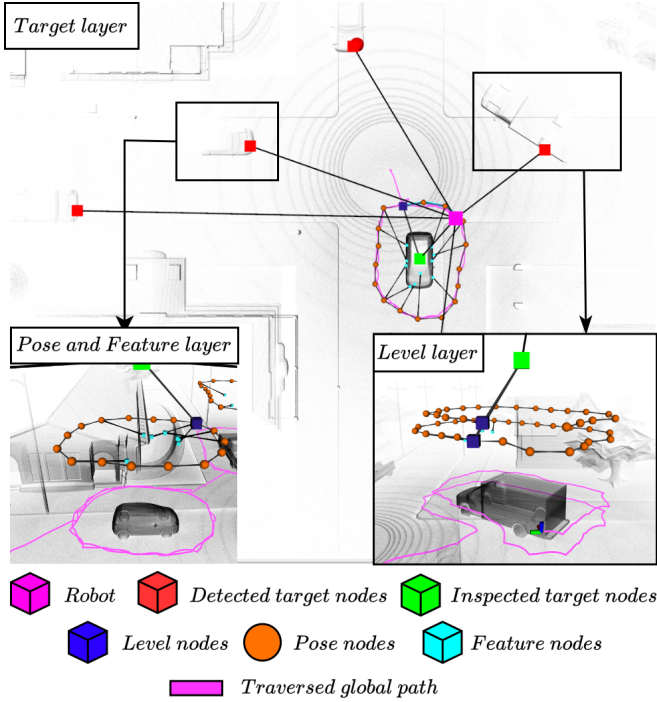


Fig. 7. A visual overview of the internal layer composition of 3D LSG constructed during a simulated inspection mission.

A. Semantic Segmentation

We deploy two purpose-specific instance segmentation models to extract relevant semantics observed during exploration and inspection. Since we enforce the use-case of inspecting semantic targets, i.e. $\{car, truck\}$ semantics, we consider the desired semantic features during inspection to be the characteristics parts of the vehicles, such as $\{front-right-door, rear-left-door, right-mirror\}$. However, the available semantic classes in this work are taken primarily due to ease-of-implementation and can be adapted based on mission context. For example, considering the use-case example to inspect a building within the context of search and rescue missions, the relevant target semantics would then become $\{house, building\}$ and the semantics-of-interest during inspection could subsequently become $\{open-window, survivor, fire\}$.

To segment semantic targets, observed during exploration, a state-of-art YOLOv8n-seg model [31] trained on COCO-dataset [32] is utilized. For the purpose of extracting semantic characteristics of the target during inspection, we deploy YOLOv8m-seg [31] trained on a *CarParts Segmentation* dataset [33]. Both models adhere to a similar process for instance segmentation but exhibit distinct localization methodologies, as would be explained in Sec. IV-B.

Considering an observation at the k^{th} instant, the semantic segmentation sub-module processes the corresponding RGB image frame \mathcal{I}_{rgb}^k for extracting the desired semantics. The RGB image has a resolution of $(I_w \times I_h)$ of 640×480 . The segmentation output consists of a set of bounding boxes $\mathcal{B}^S = \{b_1, b_2, \dots, b_n\}$ for each observed semantic element in the RGB image. Each bounding box is described by a 2D vector $v_b = [x, y] \in \mathbb{R}^2$, in pixel coordinates representing the

box's center, the width and height of the box $w, h \in \mathbb{R}^+$, the segmented class label, the confidence of detection of semantic s^c and the binary segmentation mask s^m mapping the relevant pixel coordinates that lie within the segmented region. The segmentation output is then passed over to the semantic localization sub-module which localizes the detected semantic in 3D space.

B. Semantic Localization

We utilize two main perception modalities to help in localizing the semantics of interest. During exploration, localization of semantics takes place with the projection of 3D Lidar point-cloud $\{P\}^k \in \mathbb{R}^3$ measurements over the extracted segmentation mask (s^m) of the semantic. This is achieved by

considering the camera intrinsic matrix $\mathbf{K} = \begin{bmatrix} f_x & 0 & c_x \\ 0 & f_y & c_y \\ 0 & 0 & 1 \end{bmatrix}$

with (f_x, f_y) and (c_x, c_y) being the focal lengths and camera principle points in pixel units, the relative rotation matrix $\mathbf{R}_{lidar}^{camera} \in SO(3)$ between the 3D LiDAR sensor and the camera, the corresponding translation vector $\mathbf{t} \in \mathbb{R}^3$ and the camera distortion coefficients \mathbf{D} . Equation. (1) presents the standard formulation of projecting a 3D world point $\mathbf{P}_w \in \mathbb{R}^3$ to the pixel coordinates (u, v) given the camera intrinsic and extrinsic matrices and the distortion coefficients [34].

$$\begin{bmatrix} u \\ v \\ 1 \end{bmatrix} = \mathbf{K} \cdot [\mathbf{R}|\mathbf{t}] \cdot \mathbf{P}_w + \mathbf{D} \quad (1)$$

Equation 1 is used to output the projected image plane coordinates \mathbf{p}_l of $\{P\}^k$. Subsequently, the subset of projected points ($\mathbf{p}_l^m \subseteq \mathbf{p}_l$), corresponding to valid pixel space mapped with respect to s^m , is extracted and re-projected back to 3D space (\mathbf{P}_l^m). Ultimately, \mathbf{P}_l^m is processed further to estimate the centroid of the observations and rotated back to the world frame with respect to \mathbf{X}_{odom}^k .

During inspection, we utilize aligned depth image frame \mathcal{I}_{depth}^k to localize the semantic feature in 3D space. This is because dense depth measurements enable precise localization of cluster semantic elements which may be observed within a single RGB image frame, a task where sparse LiDAR measurements would fall behind. The localization approach follows a similar approach as indicated earlier but skips the initial projection of the earlier method since the points share the pixel coordinate frame. Once s^m is obtained, it is directly used to map relevant depth pixel coordinates $\mathbf{p}_d^m \subseteq \mathbf{p}_d$ that lie within the segmented region. Subsequently, the centroid of the observations is estimated and rotated back to the world frame. The estimated global location is then passed onto the LSG. The output of 3D localization estimates of the detected semantics, $\hat{\mathbf{X}}_{target, [x, y, z]}$ and $\hat{\mathbf{X}}_{feature}$, is passed on to LSG along with their corresponding segmentation characteristics.

Figure. 9 presents runtime visualization of desired semantic elements, extracted and localized within the constructed LSG during a simulated run. In Fig. 9(a), the detected semantic targets during exploration within \mathcal{G}_T is shown. The initial 3D position of the semantic targets correspond to the estimated

output provided by the scene processing module. Fig. 9(b)-(c) present the dense segmentation of desired semantic features observed from a view-pose during inspection. The segmented features are then subsequently localized and registered within \mathcal{G}_F of the corresponding v_p from which it was observed.

V. xFLIE: LEVERAGING HIERARCHICAL REPRESENTATION FOR AUTONOMOUS INSPECTION

In this section, we discuss in detail the implementation and deployment of xFLIE architecture towards addressing semantic-aware inspection missions in unknown environments. The xFLIE architecture comprises of a modified version of our previous inspection framework FLIE [27] and the 3D LSG constructor, both working in tandem to manage mission objectives. The proposed architecture is aimed towards building and leveraging an actionable hierarchical scene representation for inspection missions in large-scale environments. Specifically, it provides a foundation for informed decision-making, facilitates processing of semantic queries and maintains an abstract representation for intuitive understanding of the information captured during inspection. Figure. 10 provides an insight of the implemented pipeline, integrating FLIE and 3D LSG, to address semantic-aware inspection in unknown environments whilst simultaneously maintaining an intuitive environment representation.

In general, FLIE autonomy exhibits an *explore-inspect-explore* approach until there remains no further observable semantic targets within the operating environment. In this work, we modify the original *exploration* planner to perform two exploration policies : (a) the initial 360° survey of the immediate vicinity of the robot denoted as $\pi^{expl:360}$ and (b) the local exploration of the region around the inspected object denoted as $\pi^{expl:LE}$. We denote the inspection policy as π^{insp} that would be executed for each registered semantic target.

A. Exploration

Once the mission is initialized, the *exploration* planner executes $\pi^{expl:360}$ to allow the robot to observe and localize the semantic targets, with necessary metric and semantic information, within \mathcal{G}_T and create an initial database for further inspection. To ensure the presence of unique and valid

node registrations at the end of every exploration phase, we optimize the initially constructed \mathcal{G}_T before evaluating the decision to inspect. The optimization of the *Target* layer graph is performed based on the consideration of spatial proximity, the segmented characteristics of the registered nodes and the corresponding inspection status, i.e. either inspected or detected. That is, out of neighbouring detected target nodes that share a region (within a distance $d_{check}^T \leq 5$ m), the one with lower s^c and s^a is removed from the graph. Appropriately, if a detected semantic target is queried against an inspected semantic, we perform a point in polygon check to see if it lies within the bounded polygon representation of the inspected target node. The construction of the bounded polygon attribute is explained in detail in Sec. V-B. In order to address the uncertainty in the detection and segmentation of a semantic during exploration, we additionally ensure that only consistent observations of a semantic within the current field-of-view of the camera are registered within the graph. Specifically, we remove nodes where the corresponding detection of its semantic by YOLO is not available for each image frame when the object resides within the visual field-of-view. Figure. 11 presents a graphical overview of the modelled optimization of the initial \mathcal{G}_T during the exploration phase of the planner. In Fig 11(a), the unoptimized $\tilde{\mathcal{G}}_T$ graph comprising of detected and inspected nodes is presented. The invalid/duplicate nodes are highlighted with hashed-boundary lines in Fig. 11(b). Figure. 11(c) presents the final pruned graph layer for subsequent evaluation of the decision to inspect.

Once \mathcal{G}_T is pruned, the nodes within the graph are ranked based on their utility and the one with maximum utility is then chosen to be inspected. The utility of $v^D \in \{v_T^D\}$ is formulated as a weighted sum of three parameters: (a) the relevance of node, which in this work is considered to be the pixel area of the segmentation with respect to image resolution $A(v^D) \in \mathbb{R}^+$. Therefore, larger semantic targets are more likely to be inspected before smaller ones. However, this can be adapted to address context of the mission, such as (i) to reflect the capability of a robot modality best suited to complete inspection, i.e. an aerial robot would be best suited to inspect buildings compared to a ground robot or (ii) prioritizing critical events for inspection, such as *car* with *smoke*

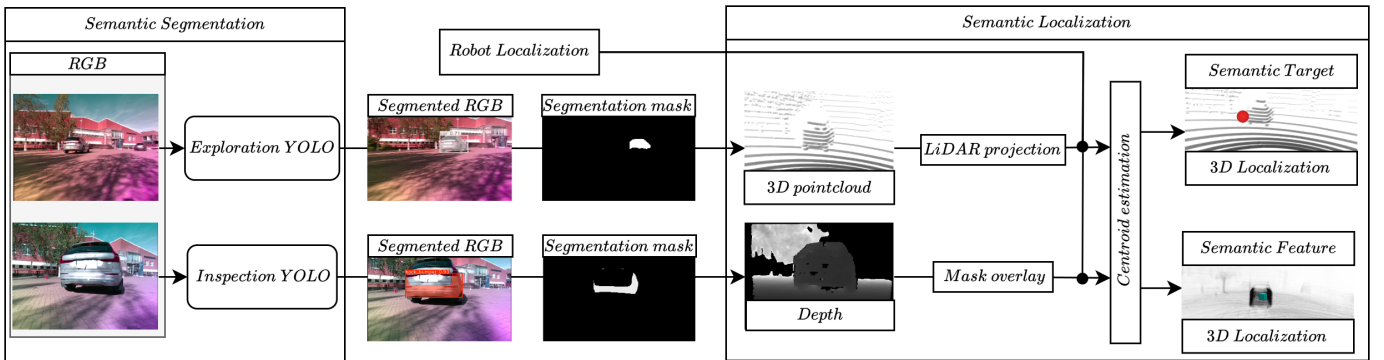


Fig. 8. A pipeline of the scene processing module responsible for detection, extraction and localization of desired semantic elements during the mission. The module subscribes to RGB, Depth and 3D LiDAR measurements, in addition to, the global robot localization estimate to extract and localize desired semantic elements within the scene.

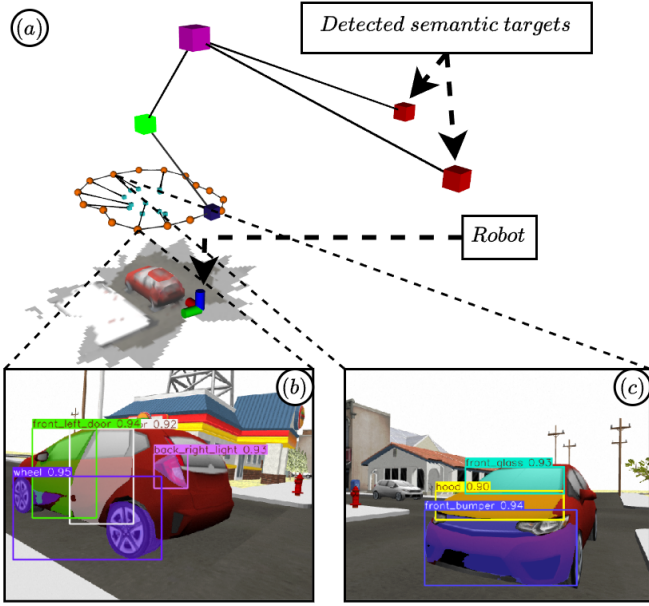


Fig. 9. A runtime visualization of 3D LSG being constructed of a car-semantic during an inspection mission in an emulated urban outdoor environment.

to be inspected first over other targets exhibiting “nominal” condition. (b) spatial proximity to other neighbouring target nodes $N(v^D) \in \mathbb{R}^+$. That is, nodes which are more central to other v_T^D nodes are prioritized to be inspected. (c) spatial proximity to the robot $P(v^D) \in \mathbb{R}^+$. Equation (2) presents the mathematical formulation of the utility heuristic function implemented to rank semantic targets for further inspection. At every necessary instant of determining the next target node to inspect, (2) is evaluated at runtime and the candidate node v^{D*} having the maximum utility is then selected for inspection.

$$v^{D*} = \underset{v^D \in \{v_T^D\}}{\operatorname{argmax}} U(v^D) \quad (2)$$

$$U(v^D) = S_p P(v^D) + S_a A(v^D) + S_n N(v^D)$$

such that,

$$P(v^D) = \frac{1}{\|\mathbf{X}_{odom[x,y,z]} - \mathbf{X}_{tgt[x,y,z]}^{v^D}\|}$$

$$A(v^D) = \frac{s_{v^D}^a}{I_w * I_h}$$

$$N(v^D) = \frac{1}{\bar{d}_{v^D}}$$

where,

$s_{v^D}^a$ is the area of the segmentation mask (in pixel units) of v^D node with I_w, I_h being the width and height of the RGB image frame and $\bar{d}_{v^D} = \frac{1}{|\{v_T^D\}|-1} \sum_{j=1, j \neq i} \|\mathbf{X}_{tgt[x,y,z]}^{v^D(i)} - \mathbf{X}_{tgt[x,y,z]}^{v^D(j)}\|$ is average distance of the current evaluated node $v^D(i)$ to other v^D nodes. $S_p, S_a, S_n \in \mathbb{R}^+$ are the weights corresponding to the three modelled parameters which influence the inspection decision. Once v^{D*} is obtained, the candidate semantic node is then subsequently communicated with the

hierarchical planner (explained in Section. V-C) to provide a traversible sequence of local paths to reach the target for π^{insp} .

B. Inspection

During inspection of the semantic target, the graphs within the remaining three layers, i.e *Level*, *Pose* and *Feature* are initialized and populated. Figure. 12 presents a visual synopsis of the top-down process of constructing and nesting of the respective layer graphs as populated by the inspection planner. The nesting of these corresponding layers along with the \mathcal{G}_T graph contributes towards the tractable nature of LSG.

As previously stated, the \mathcal{G}_L graph of the semantic target is populated based on a levels of inspection carried out by the planner. However, a highlight of the inspection planner is that it deviates from maintaining a global map representation and instead leverages the RGB frames captured during inspection to understand which part of the scene has been previously observed. Once the robot revisits a previously inspected surface within the current level of inspection, the planner proceeds to inspect the next level.

To quantify the scene similarity, we utilize a scene recognition sub-module within the inspection planner which leverages *LightGlue* [35], a neural network based local feature matcher. The consideration of a learning-based image matcher in this work overcomes the issue faced with the earlier SIFT [36] based implementation in FLIE by remaining robust against dynamic lighting conditions and varying view-pose configurations (yaw invariant) during outdoor field evaluations.

We denote $\mathcal{I}^c = \{i_1^c, i_2^c, \dots, i_N^c\}$ be the set of candidate images captured for $N \in \mathbb{Z}^+$ horizon during inspection at a level. We denote $d_{thresh}^I \in \mathbb{R}^+$ as the minimum distance between the point of initialization of the level of inspection and the point from which the scene similarity $\Gamma \in \mathbb{R}^+$ is calculated. The proximity check is done purely to limit the use of GPU-resources by the feature matcher during calculating scene similarity, which alternatively would run after the initial database of images collected. We denote $\mathcal{M}_{\mathcal{I}_q}^c | i^c \in \mathcal{I}^c$ as the matched local features between the query image \mathcal{I}_q and a candidate image i^c .

We denote $\mathcal{K}_q \in \mathbb{R}^2$ as the extracted keypoints for \mathcal{I}_q . Thus, for a given \mathcal{I}_q and \mathcal{I}^c , we find the total relative matches $\sum_{n=1}^N \mathcal{M}_{\mathcal{I}_q}^c$ obtained over the horizon with respect to the size of the queried keypoints $|\mathcal{K}_q|$. Furthermore, we normalize Γ over the size of the image set to limit the similarity score between 0 and 1. Equation. (3) mathematically formulates the implemented scene similarity scoring between a given database of images and a queried one.

$$\Gamma = \begin{cases} \frac{\sum_{n=1}^N \mathcal{M}_{\mathcal{I}_q}^c}{|\mathcal{K}_q|}, & \text{if } d_{curr}^I \leq d_{thresh}^I \\ 0, & \text{otherwise} \end{cases} \quad (3)$$

where,

$d_{curr}^I = \|\mathbf{X}_{odom[x,y,z]} - \mathbf{X}_{level[x,y,z]}\|$ and $\mathbf{X}_{level[x,y,z]}$ is the 3D position of the current level node. Figure. 13 presents a runtime snapshot of the performance of scene matching during a simulated inspection mission. Figure. 13(a) demonstrates the

matched features (colored lines) across the current and the image database populated during inspection at *Level* – 0 of a “truck” semantic. After successful recognition, the inspection planner proceeds to inspect the next level subject to meeting the vertical photogrammetric requirements defined before the mission start. In Fig. 13(b), the inspection planner reevaluates scene recognition with the updated image database for *Level* – 1. Once the planner identifies no more surfaces exist along the vertical direction, π^{insp} is terminated and $\pi^{expl:LE}$ is executed. The readers are directed towards a more detailed explanation of the inspection planning methodology presented in [27].

Once \mathcal{G}_L is initialized, populated and nested under the current target node, \mathcal{G}_P is then subsequently initialized under the current level node of inspection. The \mathcal{G}_P graph registers the tracked view-pose configuration as nodes with corresponding attributes, based on the directives of the inspection planner. Once π^{insp} is completed for $v_T^{I,curr}$, a 2D bounded polygon $\mathbb{P}^{v_T^I}$ is formed using the registered $\{v_P\} \in \mathcal{G}_P$. Each vertex in this polygon corresponds to a pose node, with its position determined by the respective node’s positional attribute. This is aimed towards assisting the autonomy to validate registration of v_T^D nodes during $\pi^{expl:LE}$. In our earlier work [27], an augmented descriptor database is utilized in conjunction with SIFT [36] for recognition of previously inspected targets. This approach was inherently sensitive to view-pose variance between the image captured during inspection and the current queried image. In addition to that, dynamic lighting conditions experienced in outdoor evaluations, such as varying overcast weather, negatively influenced the recognition performance further. Thus, by leveraging a geometric representation for identification of previously inspected targets in this work, we address the uncertainty introduced in our earlier work. Figure. 14 demonstrates an example of the above process

in action during a simulated inspection mission. Fig. 14(a) captures the instant FLIE terminates π^{insp} and switches to $\pi^{expl:LE}$. Figure. 14(b) highlights the encoded bounded polygon attribute (shown as solid *blue* area) of neighbouring inspected targets alongside the localization output from the scene processing module (shown as *red* sphere) as the previously inspected targets enter the FOV of the robot while exploring. Figure. 14(c)-(d) present individual instances where the observations are validated before being registered as v_T^D in the graph based on the geometric checks. Invalid observations are subsequently rejected and \mathcal{G}_T is updated and evaluated for v^{D*} for further inspection.

While \mathcal{G}_L and \mathcal{G}_P are populated based on planner directives during inspection, \mathcal{G}_F is populated by extracting the segmented semantics observed within the current image frame at each inspection view-pose. As the performance of semantic segmentation in real-world conditions is not ideal and involves uncertainty classifying the semantics, we maintain a preliminary unoptimized graph structure $\tilde{\mathcal{G}}_{PF}$ capturing the both the observed semantic features and the view-pose from which it was observed for each level of inspection, with each pairwise observations sharing an edge. Since a semantic feature could potentially be observed and localized in multiple view-pose configurations, we prune $\tilde{\mathcal{G}}_{PF}$ to retain only high-quality observations.

Figure. 15 presents a visual representation of the pruning process undertaken to optimize $\tilde{\mathcal{G}}_{PF}$. Figure. 15(a) presents the initial $\tilde{\mathcal{G}}_{PF}$ graph populated with semantic features with the corresponding view-pose during inspection. The graph is continuously optimized over each new set of extracted semantic features by pruning based on s_i^c and s_i^q attributes of similar feature nodes that are localized closed to each other. The modelled threshold check ($d_{check}^F \leq 1.5 \text{ m}$) filters out similar semantic nodes within proximity, among which the

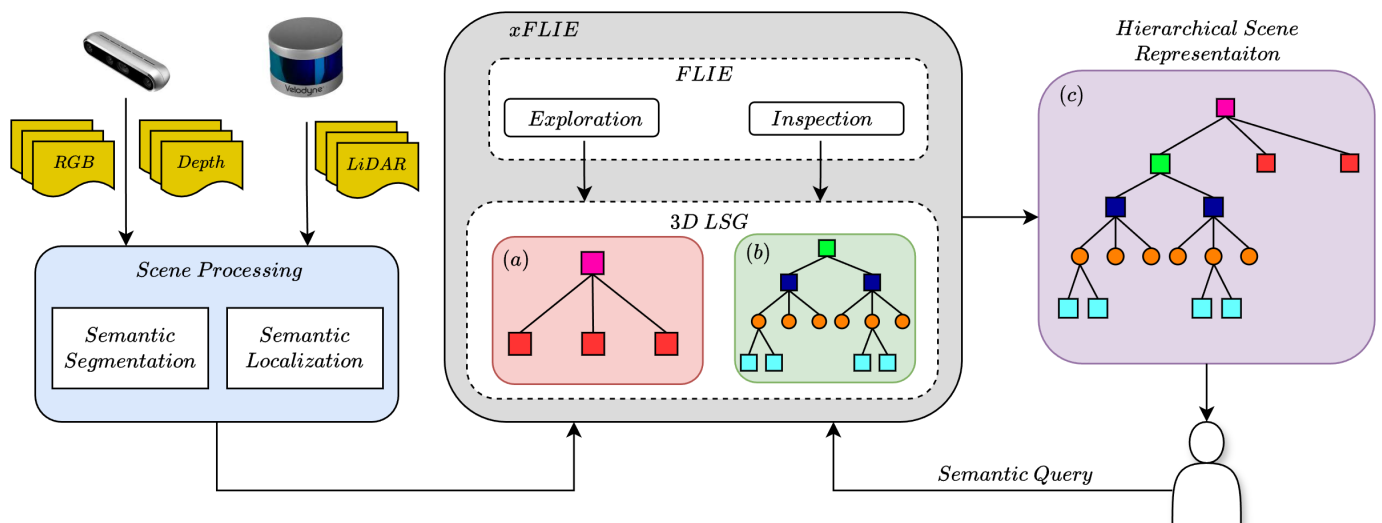


Fig. 10. The proposed multi-modal autonomy architecture xFLIE which integrates FLIE, an inspection and exploration planner, with 3D LSG, an actionable hierarchical scene representation, for semantic-aware inspection in unknown environments. xFLIE uses RGB, Depth and LiDAR measurements (shown on *top-left*) to segment and localize desired semantics during inspection and exploration. The bifurcated FLIE planner populates the corresponding layers, (a) *Target* layer during exploration and (b) *Level, Pose, Feature* layers during inspection, within 3D LSG and outputs (c) an actionable hierarchical scene representation which is used for addressing planning and semantic queries.

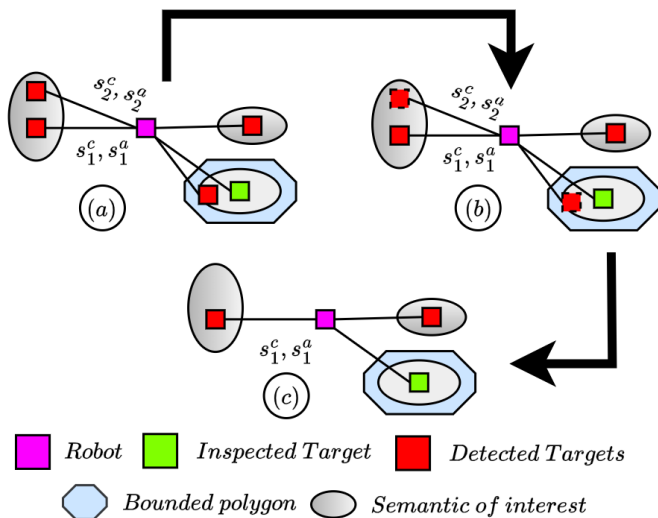


Fig. 11. A visual representation of the optimization process of \mathcal{G}_T graph after an exploration phase. In (a), the initial built graph populated with all registered semantics and its corresponding attributes, (b) the pruning of low-quality or duplicate nodes (shown with *dotted* lines) within the graph and finally (c), the filtered graph with relevant registrations of semantics-of-interest observed during exploration.

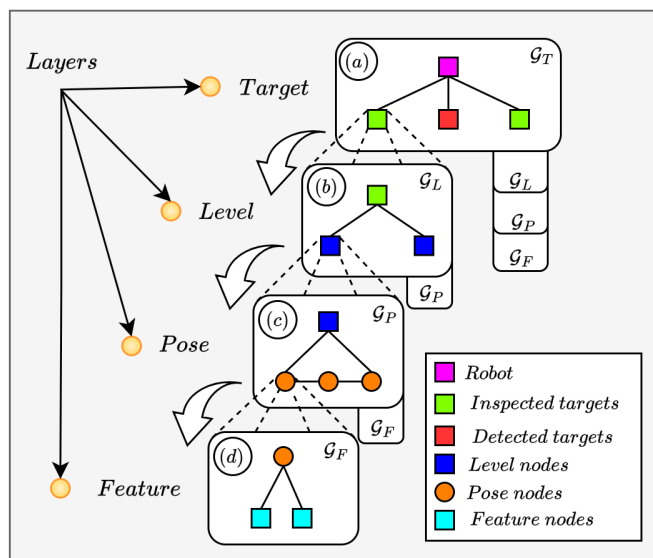


Fig. 12. A graphical representation showcasing insight into the top-down construction of the *Target*, *Level*, *Pose* and *Feature* layer graphs of LSG. (a) presents the *Target* layer graph with the populated with target nodes (v_T). In (b) the *Level* layer graph is initialized, populated with the nodes (v_L) capturing the levels of inspection and nested as an attribute of the target node under inspection, (c) for every level of inspection, *Pose* layer graph is initialized, populated with the nodes (v_P) capturing the tracked view-pose configuration as commanded by the planner and nested as an attribute under the current level node and finally, (d) for every tracked view-pose configuration, the *Feature* layer graph is initialized and populated with nodes (v_F) capturing the segmented semantics for the scene and nested as an attribute of the respective pose node.

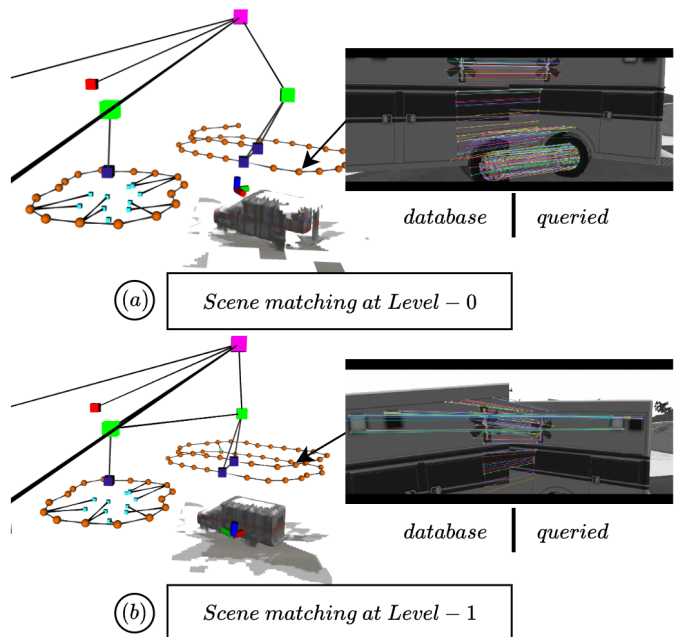


Fig. 13. A runtime snapshot presenting the performance of implemented scene recognition module during inspection of an *ambulance* in the simulated urban environment. In (a) the scene similarity is calculated at *Level - 0* to check for previously inspected surfaces between the image database collected and the current observed image. Once the scene similarity crosses the threshold, the planner continues to inspect the next level subject to visibility of the surface beyond the vertical overlap distance. In (b) the scene similarity is once again calculated for *Level - 1* and inspection is terminated when no further vertical surface regions were observed. The matched features across the images are shown via the colored lines.

one with higher attribute values is kept while pruning the rest, along with the shared edge and the corresponding pose node. Figure. 15(b) shows the pruned candidate nodes and edges after the process. Figure 15(c) presents the optimized \mathcal{G}_{PF} graph after the pruning process. Subsequently, at the end of inspection of a level, the final optimized \mathcal{G}_{PF} is deconstructed into individual \mathcal{G}_F graphs, each preserving the local subset of semantic features and nested within the associated pose node from which it was observed.

C. Hierarchical and Semantic Path Planning

Hierarchical Path Planning: One key advantage of a hierarchical environmental representation is its ability to enable fast and efficient planning [4], [8], [37] compared to conventional volumetric methods. In this work, we leverage a 3D hierarchical representation for path-planning tasks, extracting traversable paths across various layers. We also show how user-queried semantic tasks can be mapped into hierarchical planning responses, taking advantage of abstract concepts embedded within the scene representation. Instead of querying the robot to navigate to a specific metric coordinate, users can issue commands based on semantic concepts, such as instructing the robot to visit a semantic feature like *hood-1* in *Level-0* of an inspected target (e.g., *car-1*).

The hierarchical planner operates to provide a traversible path for a robot to navigate through an environment by manipulating the LSG in response to a query. The query

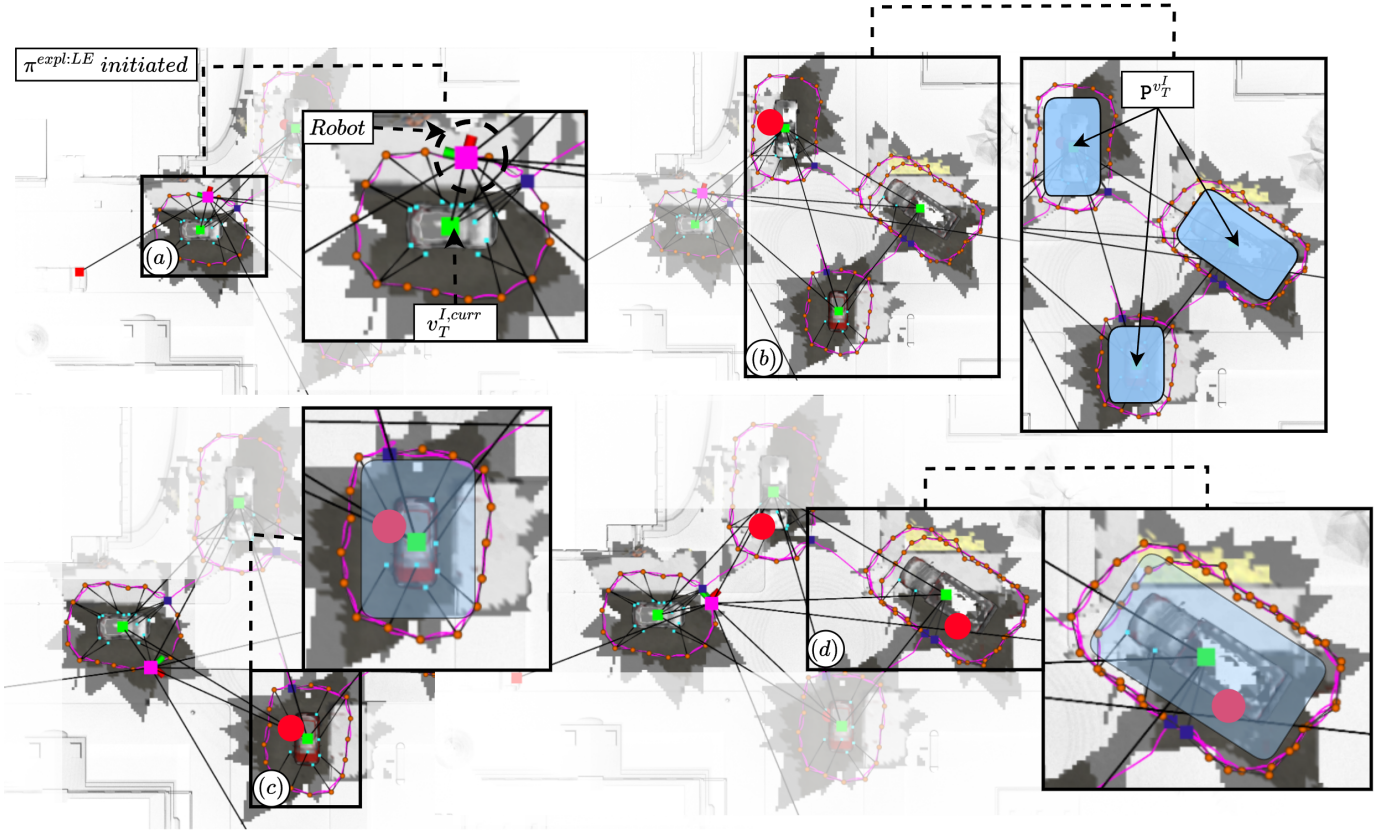


Fig. 14. A visual representation of the implemented polygon-based containment for checking and validating unique semantic target observations during local exploration. (a) sets the foundation of a scenario wherein a previously inspected semantic target is observed during local exploration around the current target node, (b) presents the detection and localization of semantic targets by the scene processing module (indicated by the *red* colored sphere) and the bounding polygon (shown as the solid *blue* area) attribute of the inspected semantic targets. (c)-(d) showcases the instant of validating the current observation through the point-in-polygon check of inspected targets that lie within the FOV of the robot.

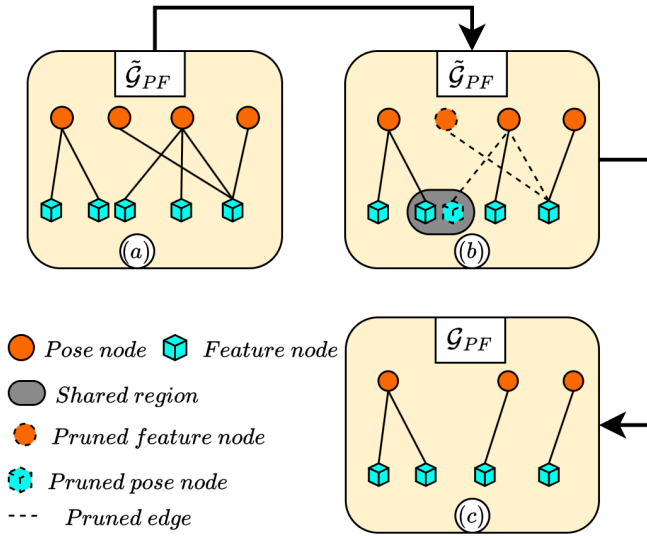


Fig. 15. The optimization process of the interim $\tilde{\mathcal{G}}_{PF}$ graph constructed during inspection of a semantic target. In (a) the graph is initially populated with the pairwise pose-feature observations, (b) presents the pruning of low-quality feature nodes and duplicate pose nodes and (c) shows the final optimized graph retaining relevant subset of pose and feature layer nodes which is later processed and nested as local \mathcal{G}_F for each pose node in \mathcal{G}_{PF} .

can originate either by the integrated FLIE autonomy stack, i.e to reach v^{D^*} for inspection or from an operator, i.e to observe *hood-1* of a particular inspected target. Specifically, the planner is designed to effectively manipulate the internal nested architecture of LSG in order to extract and expose traversible local layer graphs to a graph-based path-planner. We implement Dijkstra's graph-based path-planner in this work [38]. Upon registering a query, the planner initially localizes the robot within \mathcal{G}_T and its corresponding \mathcal{G}_L and \mathcal{G}_P to retrieve the current target node $v_T^{I,curr}$, the current level node v_L^{curr} and the current pose node v_P^{curr} respectively. Subsequently, a high-level global route ($R\{v_T^{I,curr}, v_T^{I,dst}\}$) is planned across \mathcal{G}_T . $v_T^{I,dst}$ is determined based on the nature of the query. For example, if the robot is required to reach v^{D^*} for inspection, directly implementing Dijkstra's algorithm on \mathcal{G}_T is not feasible as v^{D^*} is only connected with the parent node and is not yet fully integrated in the graph. To resolve this, the planner extracts the closest v_T^I to v^{D^*} ($v_T^{I,dst} \in \{v_T^I\}$) through a nearest neighbour search over $\{v_T^I\}$ based on the estimated location of the queried node and the encoded 3D positional attribute of inspected nodes. The global route serves as a shortest sequence of interconnected v_T^I from the robot's current position in \mathcal{G}_T to $v_T^{I,dst}$. However, the robot does not directly track this global route. Instead, the route serves as an iterable sequence of intermediate nodes, which the planner

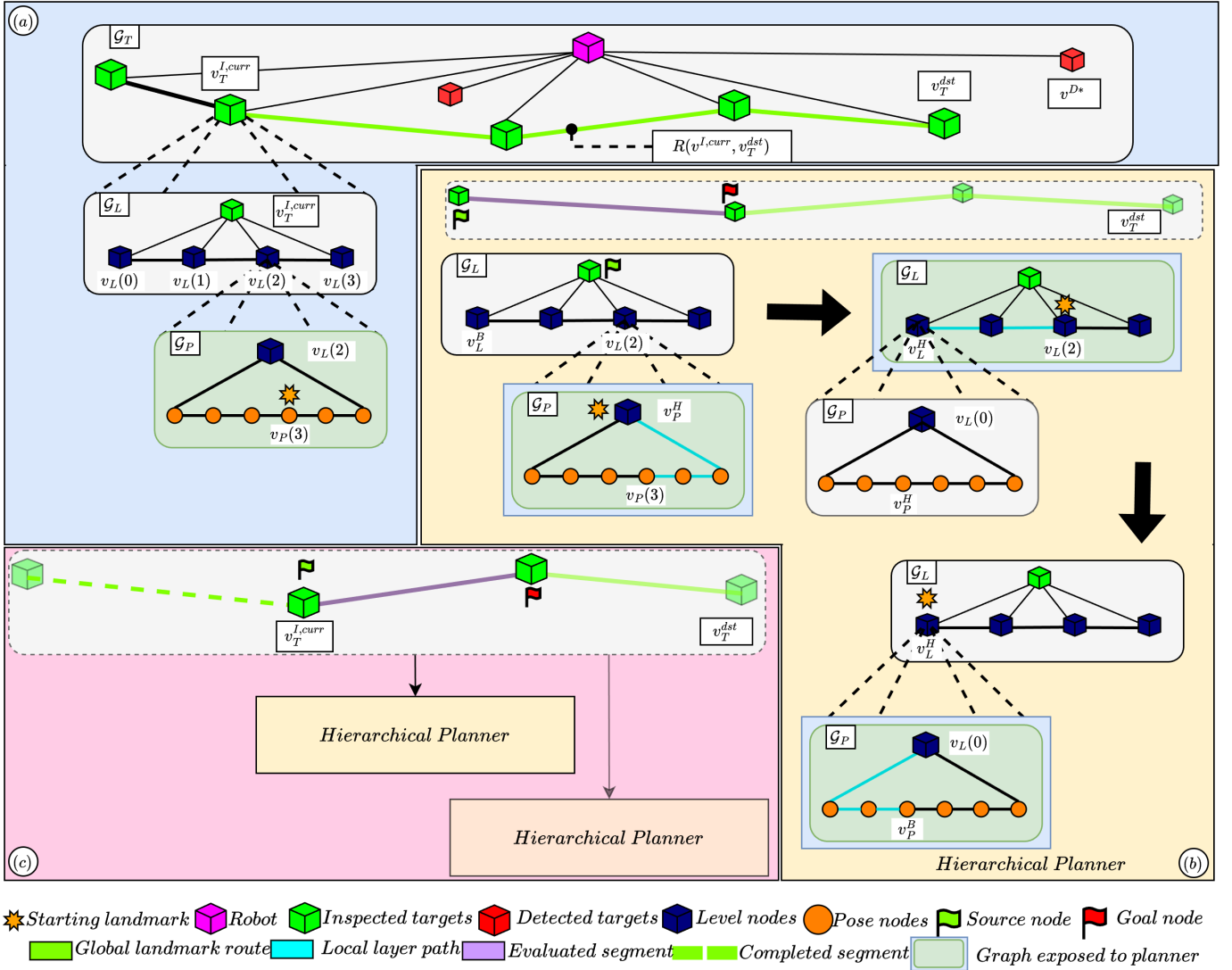


Fig. 16. A step-by-step graphical overview of the internal process of the implemented hierarchical path-planner. After registering an inspection query to reach v^{D*} for inspection and subsequently generating the global landmark route sequence $R(v_T^{I,curr}, v_T^{dst})$, (a) shows the initial step of localizing the robot across the *Target*, *Level* and *Pose* layer graphs. Once localized, (b) presents a sequence of traversal out of and across local layers through the evaluation of the layer frontier nodes. Once at the bridge pose node in $v_L(0)$, (c) indicates the recursive nature of the planner wherein the next segment of the landmark route is evaluated for traversal and continues until the robot arrives at v_T^{dst} .

uses to extract the nested local layer graphs and passes them to the path-planner. Particularly, $R\{v_T^{I,curr}, v_T^{I,dst}\}$ is evaluated in segments, where in each segment a traversible local path is planned across the current v_T^I to reach the next step in the sequence. Figure. 16 presents a graphical illustration of an instance of hierarchical planning where in Fig. 16(a) the initial step of localizing the robot and planning a global route is highlighted. Algorithm. 1 presents a pseudocode of the implemented hierarchical planning framework that manipulates the nested graph architecture in real-time to address planning queries.

For the purpose of planning across nested layers, the planner leverages the concept of layer frontier nodes (v_L^H), initially discussed in Sec. III-A. Considering the above scenario where the robot is required to reach the next v_T^I node in sequence from its current position in the graph, we consider a set of

local frontier goal nodes, v_L^H for *Level* and v_P^H for *Pose* layer graphs, that the robot has to traverse through to reach its destination. Since the graph structure within each layer is local and isolated, frontier nodes act as connectors, enabling the planner to transcend out of and navigate across various layers. This is achieved by expanding the encoded attribute of the frontier nodes and revealing the corresponding graph structure to the path-planner. Figure. 16(b) highlights a specific segment (shown as solid purple line) of hierarchical planning, executed to reach the next landmark node (indicated via the red flag) in $R\{v_T^{I,curr}, v_T^{I,dst}\}$ sequence from a current node (shown via green flag). Considering the current level node as $v_L(2)$ and the current pose node as $v_P(3)$ when the query is processed, v_L^H and v_P^H is evaluated to reach the defined v_L^B and v_P^B . In this work, we consider $v_L^B = v_L(0)$, i.e the first level of inspection, as the bridge level node with the

Algorithm 1: Hierarchical Planning Operation

Input: Target layer graph \mathcal{G}_T , Odometry $\mathbf{X}_{odom[x,y,z]}$, $\{v_T^{trm}, v_L^{trm}, v_P^{trm}\}$

/* Extract global landmark route */

$v_T^{I,curr}, v_T^{I,dst}, v_L^{curr}, v_P^{curr} \leftarrow$
 $ProcessGraph(\mathcal{G}_T, \mathbf{X}_{odom[x,y,z]}, v_T^{trm});$

$R(v_T^{I,curr}, v_T^{I,dst}) \leftarrow DijkstraPath(\mathcal{G}_T, v_T^{I,curr}, v_T^{I,dst});$
 $k \leftarrow 0;$

while not $v_T^{I,curr} == v_T^{I,dst}$ **do**

$v_T^{I,tgt} \leftarrow R(v^{src}, v^{dst})[k + 1];$
 PlanLocalPathSegments
 ($v_T^{I,curr}, v_L^{curr}, v_P^{curr}, \mathcal{G}_T, v_T^{I,tgt}$);
 $k ++;$

/* Navigate to terminal level and pose nodes */

$\mathcal{G}_L, v_L^H \leftarrow GetAttributes(\mathcal{G}_T, v_T^{I,curr}, v_L^{trm});$
LevelLayerPath ($v_T^{I,curr}, v_L^{curr}, v_L^H, \mathcal{G}_L$);
 $\mathcal{G}_P, v_P^H \leftarrow GetAttributes(\mathcal{G}_L, v_L^{curr}, v_P^{trm});$
PoseLayerPath ($v_L^{curr}, v_P^{curr}, v_P^H, \mathcal{G}_P$);

Procedure PlanLocalPathSegments():

 /* Plan local traversible paths */

$\mathcal{G}_L, v_L^H \leftarrow GetAttributes(\mathcal{G}_T, v_T^{I,curr}, v_L^B);$
 LevelLayerPath ($v_T^{I,curr}, v_L^{curr}, v_L^H, \mathcal{G}_L$);
 $\mathcal{G}_P, v_P^H \leftarrow GetAttributes(\mathcal{G}_L, v_L^{curr}, v_P^B);$
 PoseLayerPath ($v_L^{curr}, v_P^{curr}, v_P^H, \mathcal{G}_P$);

Procedure LevelLayerPath ($v_T, v_L, v_L^{tgt}, \mathcal{G}_L$):

 /* Extracts the traversible path across the Level layer */

while not $v_L == v_L^{tgt}$ **do**

while not $v_L^{curr} == v_P^{curr}$ **do**

$\mathcal{G}_P, v_P^H \leftarrow GetAttributes(\mathcal{G}_L, v_L^{curr}, v_L^{curr});$
 PoseLayerPath ($v_L^{curr}, v_P^{curr}, v_P^H, \mathcal{G}_P$);
 $R(v_L^{curr}, v_L^{dst}) \leftarrow DijkstraPath(\mathcal{G}_L, v_L^{curr}, v_L^{tgt});$
 /* Execute path */

Procedure PoseLayerPath ($v_L, v_P, v_P^{tgt}, \mathcal{G}_P$):

 /* Extracts the traversible path across the Pose layer */

while not $v_P^{curr} == v_P^{tgt}$ **do**

$R(v_P^{curr}, v_P^{dst}) \leftarrow DijkstraPath(\mathcal{G}_P, v_P^{curr}, v_P^{tgt});$
 /* Execute path */

Function GetAttributes ($\mathcal{G}, v^{curr}, v^{tgt}$):

 /* Extracts nested attributes */

$\mathcal{G}_l \leftarrow ExtractNestedGraph(v^{curr}, \mathcal{G});$
 $v_l^{curr} \leftarrow GetCurrentNode(\mathcal{G}_l, \mathbf{X}_{odom[x,y,z]});$
 $v_l^H \leftarrow EvaluateFrontierNode(v_l^{curr}, v^{tgt}, \mathcal{G}_l);$
 return \mathcal{G}_l, v_l^H

corresponding v_P^B within the nested \mathcal{G}_P evaluated through a nearest neighbour search relative to the location of the next landmark node. Once $R\{v_T^{I,curr}, v_T^{I,dst}\}$ is planned, v_L^H and v_P^H is determined based on the need to reach the bridge nodes (referred as *EvaluateFrontierNode()* function in Alg. 1). The first sequence in Fig. 16(b) presents the processing of \mathcal{G}_P based on the evaluated v_P^H to move out of the current local *Pose* layer into the *Level* layer. The planned local layer path is shown via the solid cyan colored line. The second sequence highlights local path planned across \mathcal{G}_L to reach $v_L(0)$ from $v_L(2)$ as the planner transition into the parent layer of v_P^H . The third sequence in Fig. 16(b) demonstrates the final step, expanding the encoded attribute of v_L^H and transitioning into the nested *Pose* layer graph. Subsequently, the evaluated bridge pose node and \mathcal{G}_P is then fed to the path-planner to generate the local path (shown as cyan line) for the robot to track. Once at the bridge pose node, the planner transitions out of the current target node and into the next. The above process recurses until the robot arrives at the queried nodes (shown in Fig. 16(c)). In case of a inspection query, once the robot arrives at the bridge pose node, i.e. the terminal pose node, of $v_T^{I,dst}$, π^{insp} is executed and the corresponding layers within LSG is populated. If a specific semantic feature at a certain level must be visited, the planner evaluates and processes the nested layer graphs subject to the terminal nodes that needs to be reached.

Semantic Path Planning: 3D LSGs maintains an intuitive scene representation of semantic concepts over multiple layers of abstraction. This makes it a powerful tool that can be leveraged to address semantic tasks which can extend the lifetime of an inspection mission. Using the registered semantic labels, an operator can quickly process the constructed 3D LSG and command a robotic platform to visit a semantic-of-interest. The semantic-query take the form of: “Visit v_F in v_L of v_T^I ”, where v_F, v_L, v_T^I correspond to the semantic labels of the registered nodes in the final 3D LSG. The nodes are subsequently passed onto the hierarchical planner as the final terminal nodes v_F^{trm}, v_L^{trm} and $v_T^{I,trm}$ for further planning operation.

Figure. 17 highlights the planning across local layers of key landmark nodes in the global landmark route sequence to address a semantic query “ Visit *front glass-1* in *Level-1* of *truck-16* ” issued by an operator. The query is processed by mapping the semantic labels, i.e. v_F, v_L, v_T , mentioned in the query to the corresponding terminal nodes, $v_F^{trm}, v_L^{trm}, v_T^{I,trm}$. This is later fed to the hierarchical planner for providing the high-level global route and the subsequent traversible local paths, navigating across the abstraction layers and through the environment. The current location of the robot when it receives the semantic query is shown in Fig. 17(a), where in a global perspective is located the *top-left* corner of the map. Figure. 17(b) points to a zoomed in region of the queried terminal nodes. Once the necessary parameters for planning are identified, i.e. $v_T^{I,curr}, v_F^{trm}, v_L^{trm}$ and $v_T^{I,trm}$, a high-level route is initially generated across the \mathcal{G}_T , shown as the solid green line connecting $v_T^{I,curr}$ and $v_T^{I,trm}$ through a sequence of intermediate inspected targets (refer Fig. 18). The planned segments, captured at various instances, for the landmark

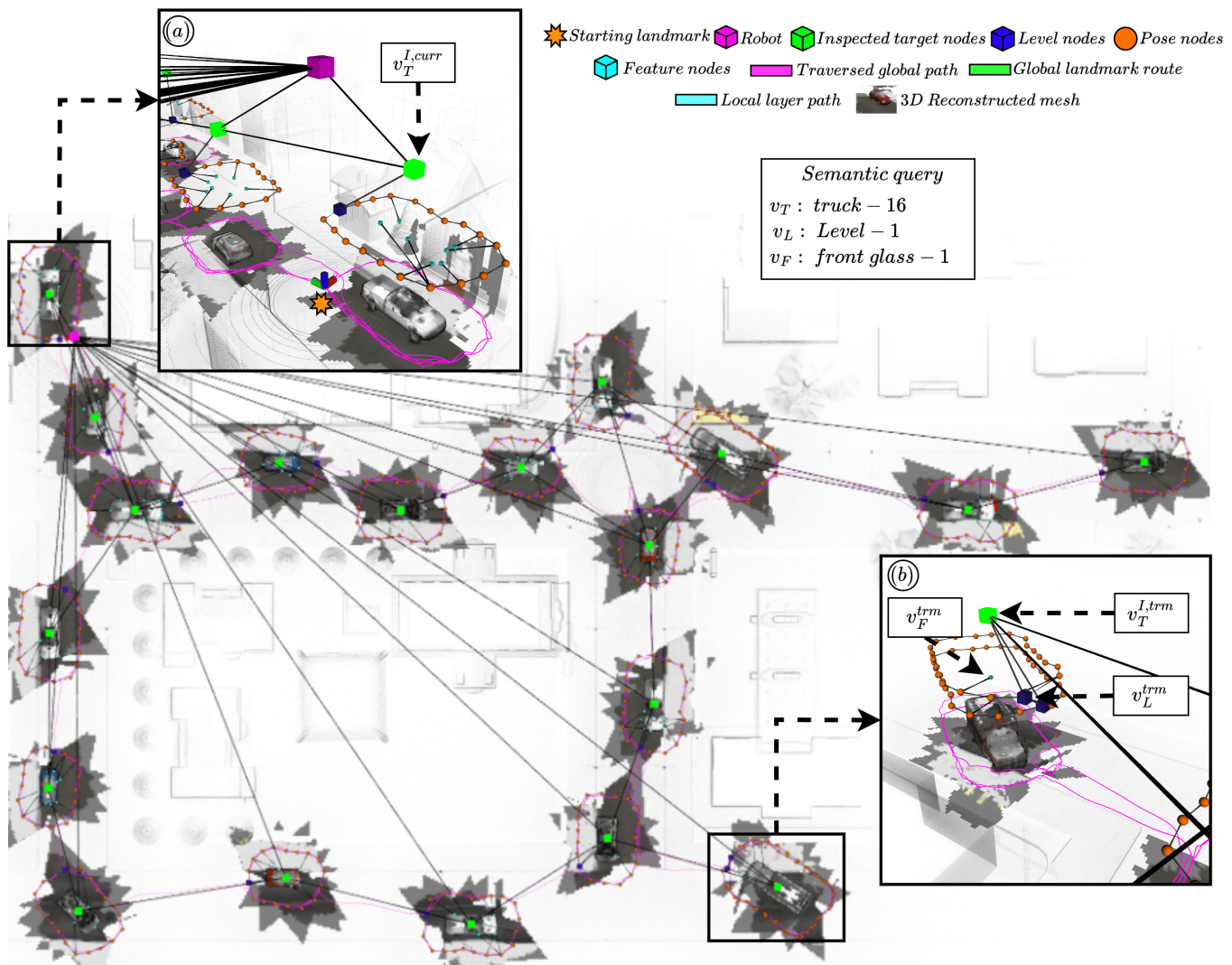


Fig. 17. A visual depiction of an executed semantic query addressed at the end of 20 vehicle simulated inspection mission. (a) presents the zoomed location of the robot when it receives the query. (b) presents a zoomed-in frame highlighting the registered terminal nodes.

nodes in the global sequence is shown in Figures. 18(a)-(d). In Figure. 18 (a), the initial planned local segment is highlighted whereas Fig. 18(b)-(c) capture the response over time as the robot navigates across the environment and through the global landmark nodes in sequence. Figure. 18(d) present the final planned segment to traverse from $v_L(0)$ to v_L^{trm} at v_T^{trm} and shows the robot arriving the parent pose-node of the queried semantic feature.

VI. EVALUATION SETUP

A. Hardware and Software

In this work, we validate the proposed architecture in field trials using a fully autonomous BD Spot quadruped equipped with Nvidia Jetson Orin computational unit, Realsense D455 stereo-optical sensor, Velodyne VLP16 high-res 3D LiDAR and Vectornav VN-100 Inertial Measurement Unit (IMU). We utilize *LIO-SAM* [39] for providing localization estimates. Figure. 19 highlights the deployed autonomy sensor suite on BD Spot. Furthermore, we deploy a modified and quadruped-

compatible version of the high-level Nonlinear Model Predictive Controller (NMPC) [40] to provide directional command velocities to BD Spot's onboard low-level controller to track the view-pose references.

The xFLIE architecture is evaluated in the simulation environment using Gazebo [41] and RotorS aerial [42] simulator. One of the flavour of xFLIE is that it is platform agnostic with the only requirement that the platform be holonomic. While large-scale field deployment of aerial platform is not presented in this work, we test and execute the architecture on a simulated aerial vehicle and deploy the same on BD Spot for field evaluation. The only difference in the code between the two takes the form of an input *modality* parameter which acts to inform the inspection planner about the platform's potential in fulfilling multi-level inspection, i.e to move in Z-direction.

We use ROS Noetic with Ubuntu 20.04 as the preferred software base. The Nvidia Jetson is flashed with JetPack SDK v5.1. Additionally, we use NetworkX [43] library for graph construction. The code is written in Python v3.8 with only a PCL library [44] based voxel-grid based depth point-

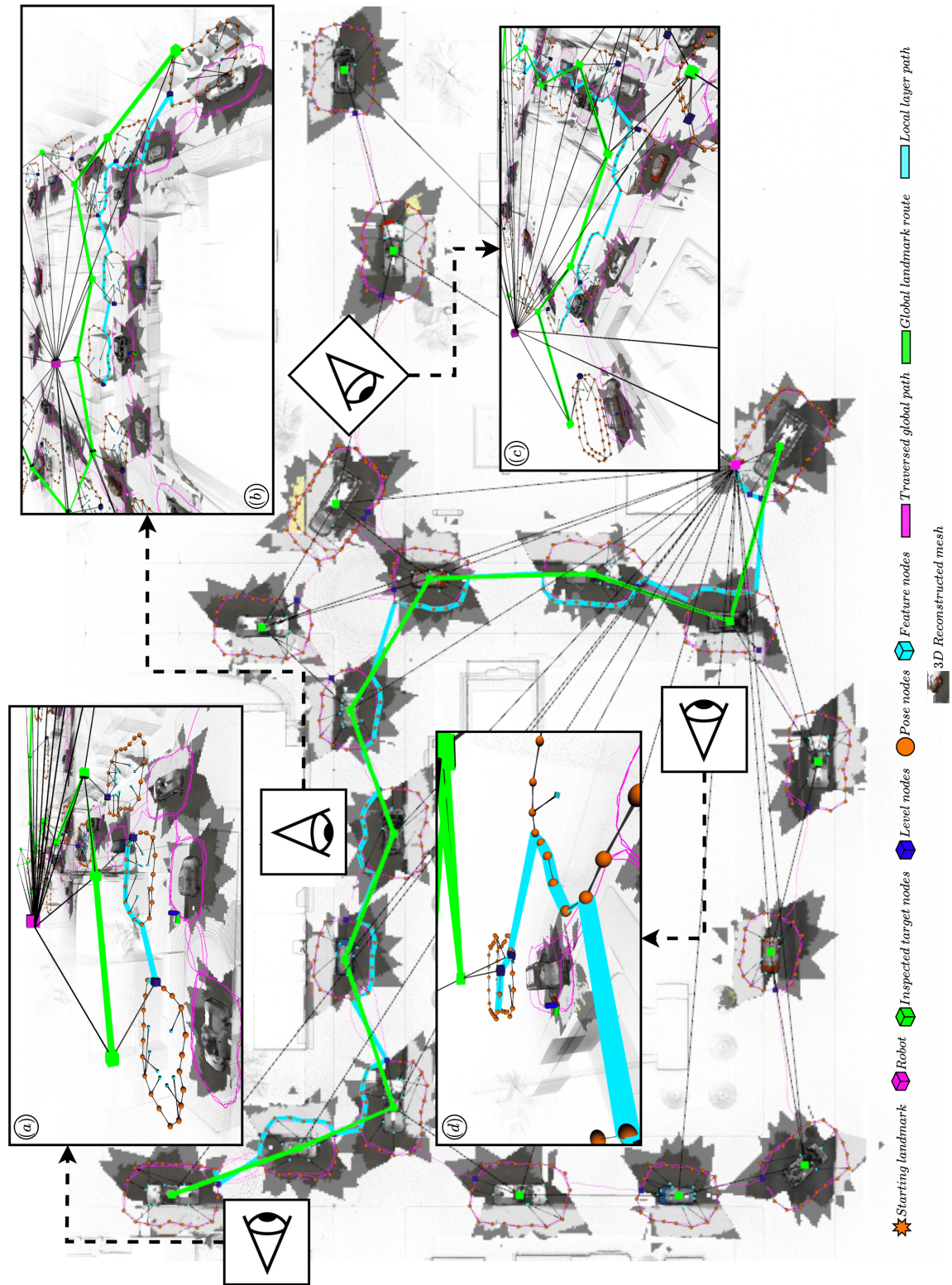


Fig. 18. A demonstration of hierarchical planning in response to an operator issued semantic query (refer Fig. 17). (In *background*) The generated global landmark route is shown in solid *green* and the generated local traversible path is shown in *cyan*. (a) presents a zoomed-in frame highlighting the local path generated to reach the next landmark node for the initial instance. (b)-(c) captures the evolution of the generated local paths enabling the robot to navigate across the environment while traversing through the global landmark sequence. (d) captures the final planned segment generating local path across the *Level* and *Pose* layers to reach the terminal pose from which the queried semantic feature was observed.

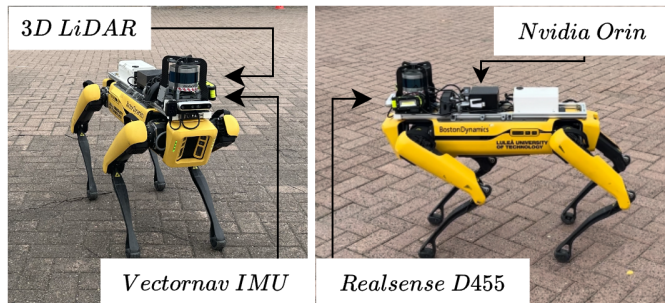


Fig. 19. A visual depiction presenting the sensor suite deployed on a Boston Dynamics (BD) Spot quadruped robotic platform for deployment in the field.

cloud downsampler written in C++. We reserve the use of GPU primarily for running YOLOv8n-seg, YOLOv8m-seg and LigthGlue models. The rest of the code including FLIE and 3D LSG runs over the CPU.

B. Simulation Scenario



Fig. 20. A top-down perspective on the urban small-city simulation environment used in Gazebo. We modified the original file to add and/or reposition additional vehicles.

Figure. 20 presents the open-source urban environment which is used for simulation evaluation of xFLIE. The environment comprises of 20 vehicles, a mixed combination between cars and trucks spread throughout the city. A video comprising of results obtained during the simulation evaluation is available online via this link, <https://youtu.be/mXNoNyuWE-0>. In this video, we showcase the inspection mission in the urban city environment. We also visualize the hierarchical and semantic path-planning operations for both planning-related as well as operator-defined queries. We also visualize the corresponding simulation video captured for the performance scalability study undertaken in this work (refer Fig. 24).

C. Experimental Scenario

We deploy the robot for inspecting vehicles within the campus ground of Luleå University of Technology, Luleå, Sweden. Figure. 21 presents the site of the field evaluations carried out in this work. While the vehicles designated for inspection were static, the scene in general was dynamic with walking humans, moving service vehicles and changing lighting conditions

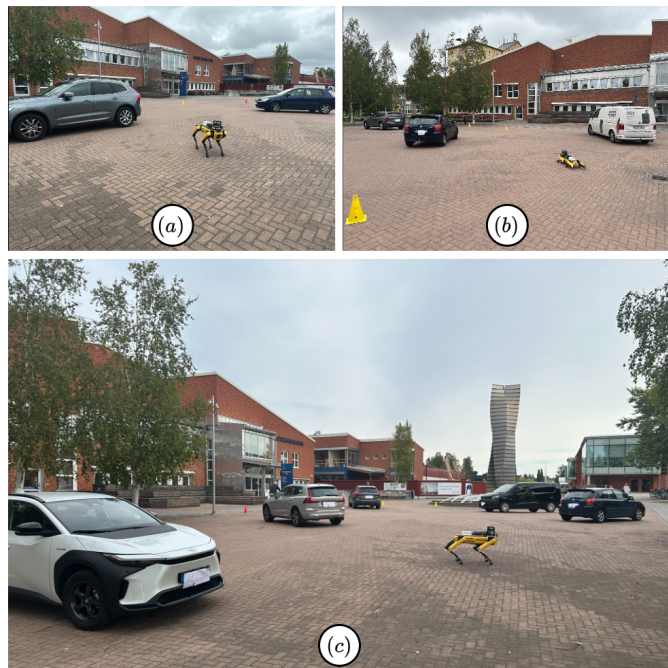


Fig. 21. A visual description of the operating environment considered for field evaluation of xFLIE architecture. The environment resides as part of Luleå University of Technology campus grounds located in Luleå, Sweden-97187. (a) presents the two vehicle inspection, (b) presents the three vehicle inspection sceanaio and (c) presents the five vehicle inspection scenario.

throughout the duration of field trials. A corresponding video capturing the results obtained during the field evaluation is available online, <https://youtu.be/zbFsfKPqoPw>. In this video, we visualize the performance of xFLIE architecture for the three evaluated scenarios. We highlight the construction and utilization of 3D LSG during autonomous inspection. We also present hierarchical path planning while addressing inspection queries for all three scenarios. However, we only demonstrate semantic path planning for the first scenario, i.e two vehicle inspection. This is because of bad performance of semantic localization due to loss of synchronization of robot odometry with corresponding point-cloud measurements observed during exploration. This in turn affected \mathcal{G}_T optimization during point-in-polygon validation. As a result, invalid registration of previously semantic targets led to manual termination of the mission.

VII. RESULTS AND DISCUSSIONS

A. Simulation Evaluation

Figure. 22 presents a collage of runtime snapshots of 3D LSG constructed at various epochs throughout the simulated run. For the simulation runs, we considered $S_p = 50$, $S_a = 5$, $S_n = 5$ as the weights for evaluating (2). Due to performance of YOLO, only 17 cars out of 20 were detected and localized successfully. However, additional runs (refer Fig. 24) showcase detection, localization and inspection of total 19 vehicles. Figures. 22(a)-(d) show the evolution of the graph topology across the different layers of abstraction. In this run, the weighted gains for calculating semantic target node utility, are assigned equal weights. Thus, the influence of the

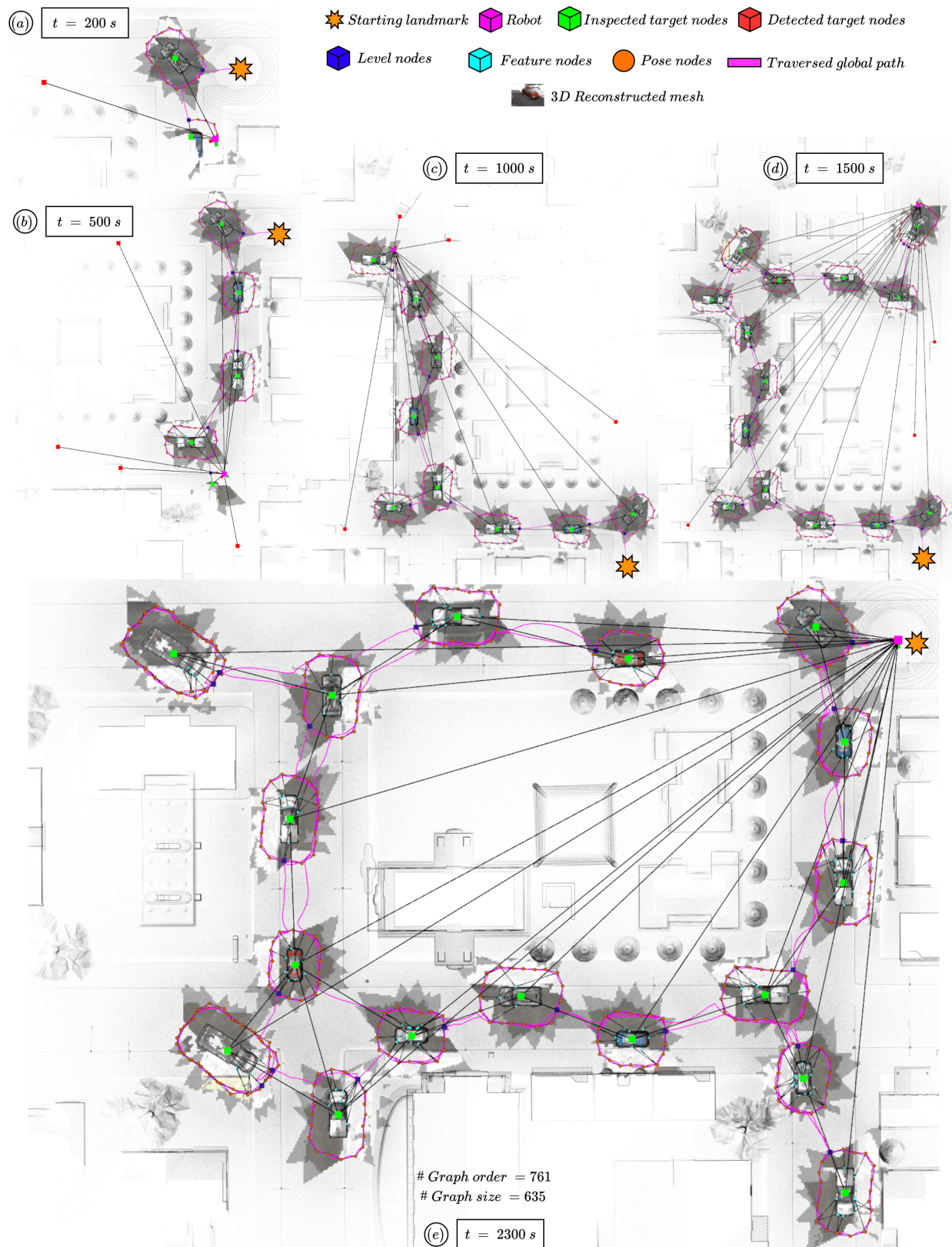


Fig. 22. A collage of runtime snapshots of the proposed architecture evaluated in the simulated *small city world* in Gazebo. Figures. 22(a)-(d) present the constructed LSG during inspection over specified epochs of 200, 500, 1000 and 1700 seconds into the mission, respectively. Figure. 22(e) presents the overall LSG constructed at the end of the simulated run. The color-coded representation of nodes in the modelled layers is given via the legend. Out of 20 semantic elements of interest located in the environment, xFLIE autonomy is able to detect, localize and complete inspection of 17 of them. The remaining 3 were not detected due to the performance of YOLO in this particular run.

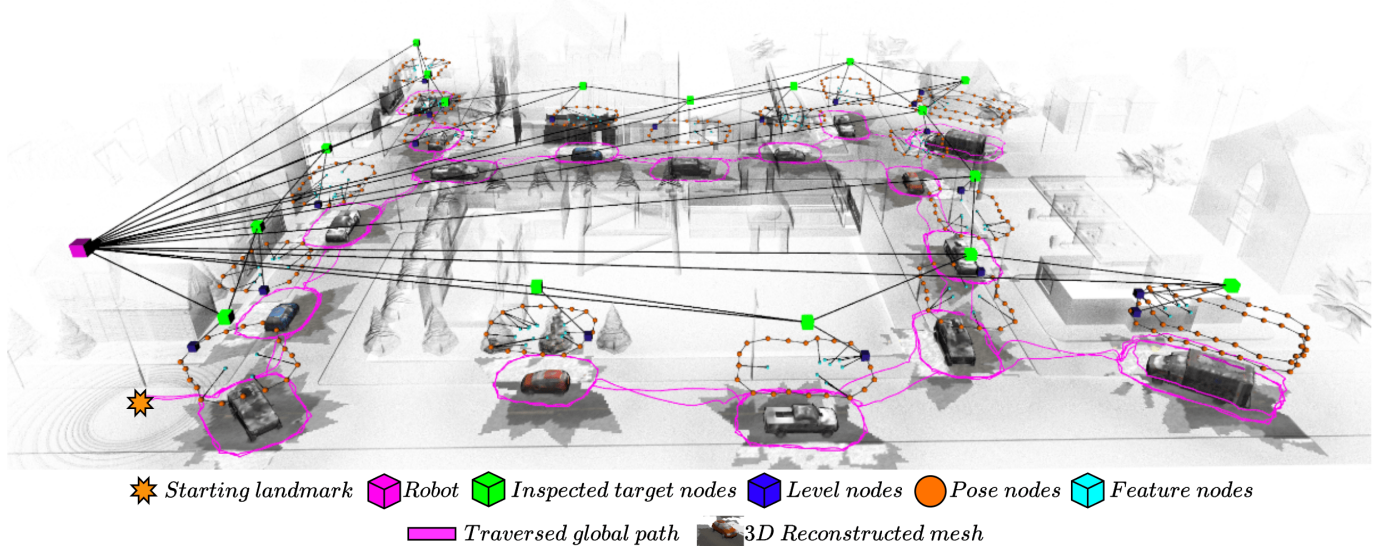


Fig. 23. A three-dimensional perspective of the final 3D LSG alongside the reconstructed 3D mesh of inspected semantic targets at the end of the simulated inspection mission. The path traversed by the robot is overlaid as the solid *pink* colored line.

spatial proximity factor dominates the decision taken to inspect resulting in the robot visiting nearby semantic targets. This can be specially seen in the sequence Fig. 22(a)-(b). At the simulation epoch of 500s, the influence of the node centrality factor, i.e. proximity to other semantic targets, rises due to the addition of two semantic targets in the same neighbourhood. This effect is highlighted in Fig. 22(d) where the planner ignores the isolated semantic target in the top-left corner of Fig. 22(c) and instead proceed to traverse towards the clustered semantic targets. Figure. 22(e) presents the final constructed 3D LSG at the end of the inspection mission which is later used to address semantic-queries.

Figure. 23 presents an overview of the outcome of the simulated inspection mission with the constructed 3D LSG alongside the reconstructed 3D mesh of inspected semantic targets. While twenty vehicles were distributed throughout the environment, the proposed architecture was able to explore, detect, localize and subsequently inspect seventeen out of twenty semantic targets. The remaining three were not detected by the utilized YOLO module thus not registered and available for further inspection. Overall, the LSG in this run has a graph size of 635 edges with a total of 761 nodes populating graphs across the various layers of abstraction.

Figure. 24 showcases a performance study into the scalability of the proposed architecture. In this study, we consider three scenarios for which the number of semantic targets located in the environment increases, with scenario 1 comprising of four vehicles, scenario 2 comprising of 10 vehicles and scenario 3 comprising of 20 vehicles. In Fig. 24(a), the variation in size of the graph, i.e. number of edges, processed by Dijkstra to plan a path is visualized across all three scenarios. The metric is recorded for every instance the hierarchical planner is queried, both by the FLIE planner as well as during semantic-queries by the operator. Due to the nested nature of LSG, Dijkstra's path planner is only exposed

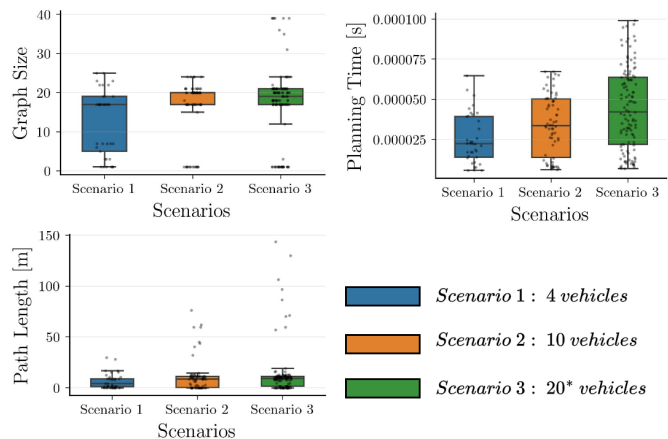


Fig. 24. A study of planning performance recorded over the three simulation scenarios of semantic-aware inspection in an urban outdoor environment.

to the local graph of the layer that needs to be traversed. This can be seen reflected in the consistent median graph size ≈ 20 which corresponds to the number of view-poses visited for a level of inspection. The distribution of the individual observations is overlaid on top of the box-plot as well. The outlier points reaching upto graph size of 40 correspond to \mathcal{G}_T being processed for a global route. Since the nodes in this layer maintain an edge with the parent node as well as a shared edge between inspected nodes, the doubling in size is expected. Figure. 24(b) presents the planning time metric captured for each instance a valid path is generated. As the number of inspected targets increases, the planning time shows a marginal increase with each run. Figure. 24(c) presents the recorded length of the path planned during the mission. This result aligns with the one in Fig. 24(a), where the planner largely traverses across the local *Pose* layer graphs. Based

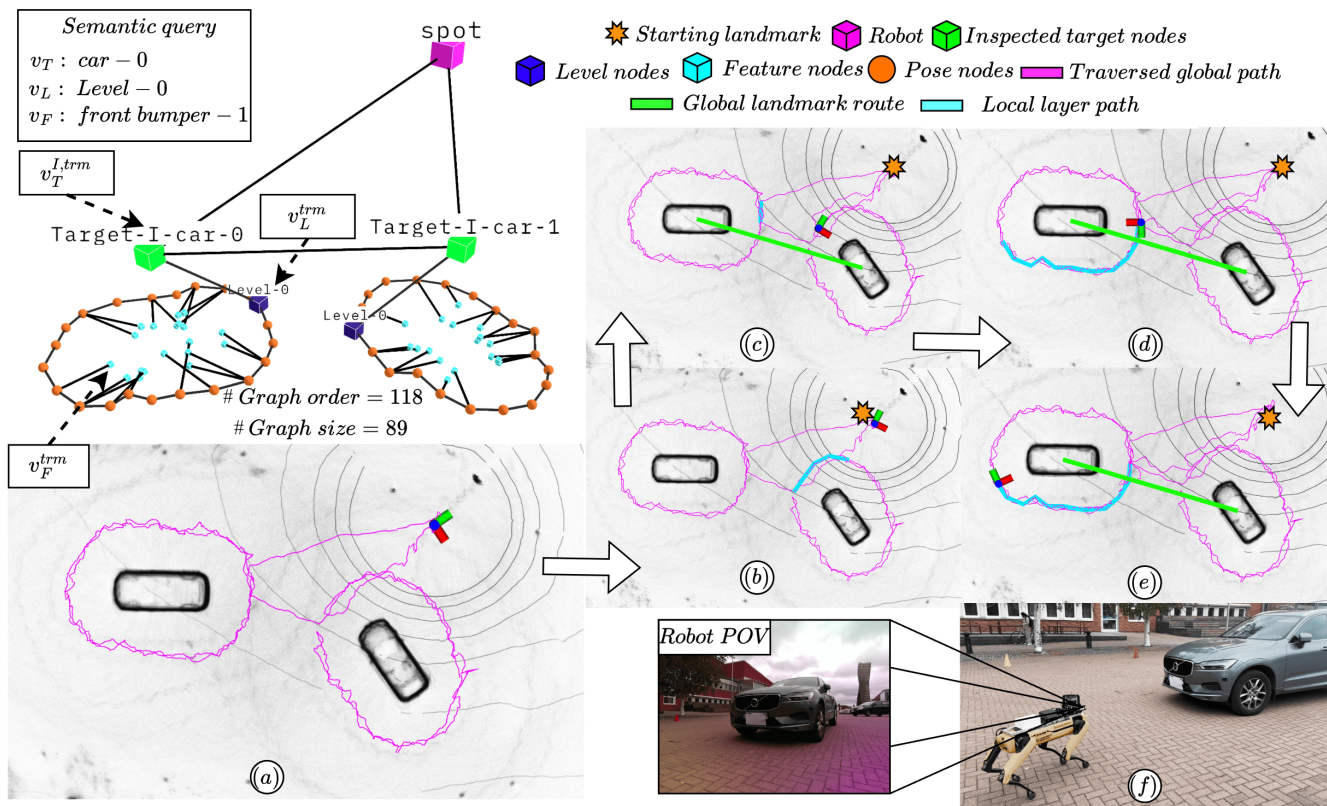


Fig. 25. A collage demonstrating the performance of the hierarchical and semantic path planning capability over LSG at the end of inspection. (a) presents the 3D LSG constructed during inspection viewed alongside the point-cloud representation of the environment. The semantic query (shown on *top-left* corner) is issued by the operator at the end of the inspection mission. (b)-(e) present a sequence of the hierarchical planning response providing a traversible route to reach the queried semantic feature *front bumper-1*. (f) presents the robot point-of-view as it maintains the required view-pose to view the semantic feature.

on the underlying observations, the *outlier* points capture the recorded path length across the *Target* layer graph which, unlike the recursive nature of planning across the local nested graphs, is executed only once for each planning query. Overall, the recorded metrics highlight the effectiveness of maintaining and planning over nested hierarchical scene representations with a marginal increase in planning time compared to almost doubling in the number of total semantic targets inspected.

B. Field Evaluation

Figure. 25 presents a field evaluation result of two-car inspection scenario along with the semantic-query executed at the end of the mission. Overall, LSG maintains a graph size of 124 with over 165 registered nodes across various layers of abstraction. At the end of the inspection mission, the operator issues a semantic query “Visit *front bumper-1* in *Level-0* of *car-0*” to the robot. Figure. 25(b)-(e) present the result of the hierarchical planning with the planned global route (shown as solid *green*) and the recursively planned local layer path (shown as solid *cyan*) to reach the queried semantic feature. Figure. 25(*bottom*) presents the robot maintaining required view-pose to observe the semantic feature. For the performance in Fig. 25 and Fig. 26, we considered $S_p = 50, S_a = 5, S_n = 5$ as the weights for the evaluating the utility of a registered semantic target.

Figure. 26 presents a compilation of the experimental results obtained for the inspection scenario of three cars alongside the constructed LSG at the end of the inspection run. In general, the proposed architecture was able to detect, localize and inspect all the semantic targets present in the environment. Figures. 26(a)-(c) provide a visual description of the vehicles in the environment designated to be inspected. Figures. 26(d)-(e) demonstrate the performance of the implemented hierarchical planner leveraging the nested LSG structure for addressing planning queries raised by the integrated FLIE autonomy. Figure. 26(f) visualizes the 3D LSG at the end of the inspection run. The extra v_T^D is an anomaly resulting due to an unsynchronized semantic localization process, where a semantic target was localized in a region where there are no vehicles. The mission was terminated at the end of the inspection of the three vehicles. Figures. 26(g)-(i) provide an example output of the segmentation of observed semantic features for registration within $\tilde{\mathcal{G}}_{PF}$ during inspection.

Figure. 27 presents the outcome of the field evaluation carried out for the five vehicle inspection scenario. In this run, we ran the experiment with $S_p = 50, S_a = 5, S_n = 200$ weights for evaluating (2). The 3D LSG constructed during the inspection mission is shown in Fig. 27(a) while a top-down perspective of point-cloud map of the environment is shown in Fig. 27(b). Overall, the autonomy was able to detect, localize and inspect all five semantic targets along with

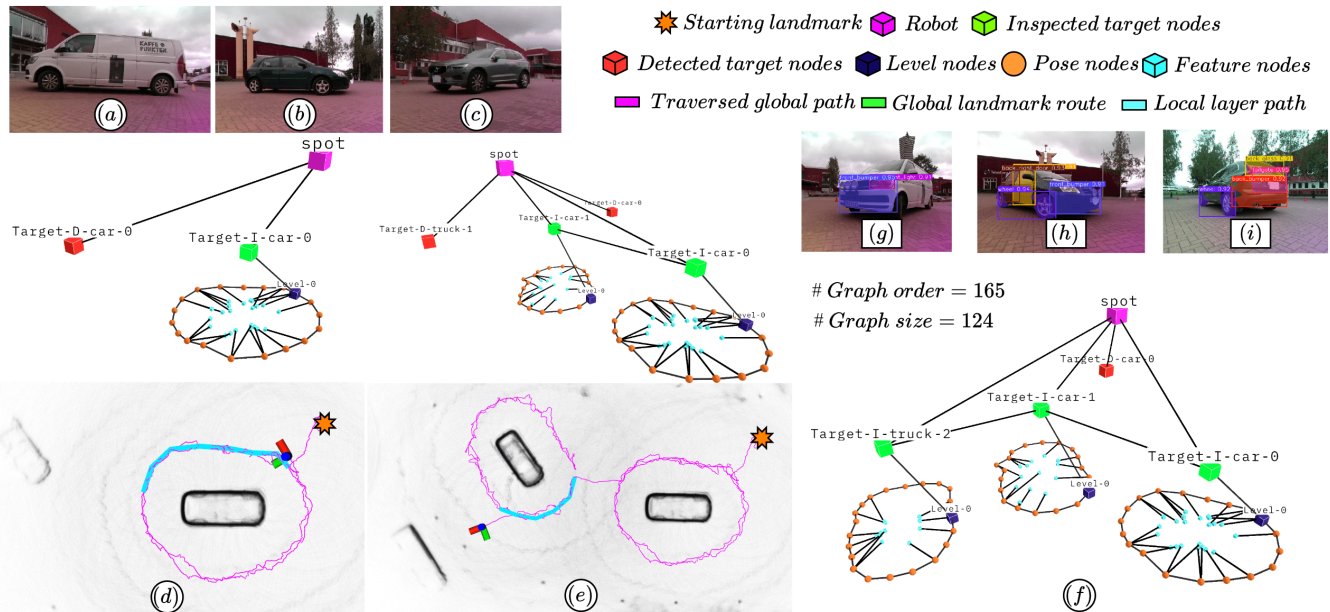


Fig. 26. Visualization of experimental results obtained during three vehicle inspection scenario. (a)-(c) presents the different vehicles located in the operating environment. (d) presents the outcome of hierarchical planning in response to a planning query to navigate towards *Target-D-car-0* for further inspection. In (e), another instance of leveraging 3D LSG by the FLIE autonomy for path-planning tasks is shown, (f) presents the 3D LSG constructed during the evaluated inspection mission. (g)-(i) shows snapshots of the performance of the onboard segmentation model to detect and extract desired semantic features observed during inspection of semantic targets observed in the environment.

their corresponding characteristic semantic features within the LSG. The effect of the influence of S_n on the decision to inspect can be observed in clarity within the associated field evaluation video (refer Sec.) for the current scenario. For instance, the robot, after inspection of “*Target-I-car-0*”, proceeds to inspect the distant “*Target-I-car-2*” as a result of the presence of duplicate detected target node in proximity to the inspection target (refer to the dual semantic target nodes in close-proximity in *middle left* of Fig. 29(e)). Thus, increasing the overall $N(v^D)$ of the evaluated semantic target compared to the rest. Subsequently, the autonomy directs the robot to the far-away semantic target instead of the one available next to its current position. While the implemented optimization safeguards removed most of the redundant registration, thereby maintaining the quality of the \mathcal{G}_T graph, the process failed to remove the duplicate node in this outlier case.

Figure. 28(a) presents the performance of the hierarchical planner when queried by FLIE to navigate towards v^{D*} , i.e. “*Target-I-truck-3*” semantic label in Fig. 27(a), for further inspection. The planned global route is indicated via the solid *green* line whereas the local layer path is shown as solid *cyan* line. Figures. 28(b)-(d) present the executed local path segments in order, navigating across the landmark node sequence to reach the final v_P^{trm} of $v_T^{I,dst}$ to start inspection. Figure. 28(e) shows the robot arriving at v_P^{trm} after tracking the local path segment and subsequently initiating inspection.

Figure. 29 presents a collage comprising of different instances where the constructed \mathcal{G}_T during the experimental evaluation for a five vehicle inspection is optimized and pruned of duplicate and low-quality registration of observed semantic targets. The initial \mathcal{G}_T constructed at the end of $\pi^{expl:360}$ after initialization of the mission is shown in Fig. 29(a). The effect

of delay between the processing of RGB image by YOLO and the subsequent localization of the semantic target based on the robot’s localization estimate \mathbf{X}_{odom} is highlighted by the bold *dotted* circle. This is due to continuously updated pose of the robot at it executes $\pi^{expl:360}$. Thereby losing synchronization with the registered RGB image and the corresponding 3D point-cloud measurements leading to an incorrectly estimated $\hat{X}_T^{v^D}$. However, such events are effectively handled during the final \mathcal{G}_T update. Figures. 29(b)-(c) present a timeline of inspecting v^{D*} , evaluated after $\pi^{expl:360}$ (refer Fig. 29(b)), and the subsequent update of the initial estimated $\hat{X}_T^{v^D}$ to align with the centroid of \mathbb{P} constructed around $v_T^{I,curr}$ after inspection (refer Fig. 29(c)). Figure. 29(d)-(e) present a runtime sequence highlighting the polygon-based node validation process. During $\pi^{expl:LE}$ around v_T^I , \mathcal{G}_T registers new observed semantic targets (seen in Figure. 29(d)) with the subsequent π^{insp} policy being executed afterwards, presented in Fig. 29(e). Finally, Fig. 29(f) presents an instance of pruning a duplicate node via a point-in-polygon check, registered during exploration but located within a restricted region around an inspected target.

Figure. 30 presents the recorded metrics of hierarchical planning evaluated for the three experimental scenarios. The observation points (seen in *grey* circles) are overlaid against the box-plots. The presented metrics consists of addressed planning and semantic queries for Scenario 1 and Scenario 2 and only planning queries for Scenario 3. This was due the registration of the anomalous phantom nodes, as explained earlier, causing FLIE to continue with inspection. As a result, the experiment was terminated and semantic queries were not possible to issued. The recursive behaviour of the hierarchical planner as it extracts and plans over local \mathcal{G}_P and \mathcal{G}_L graphs

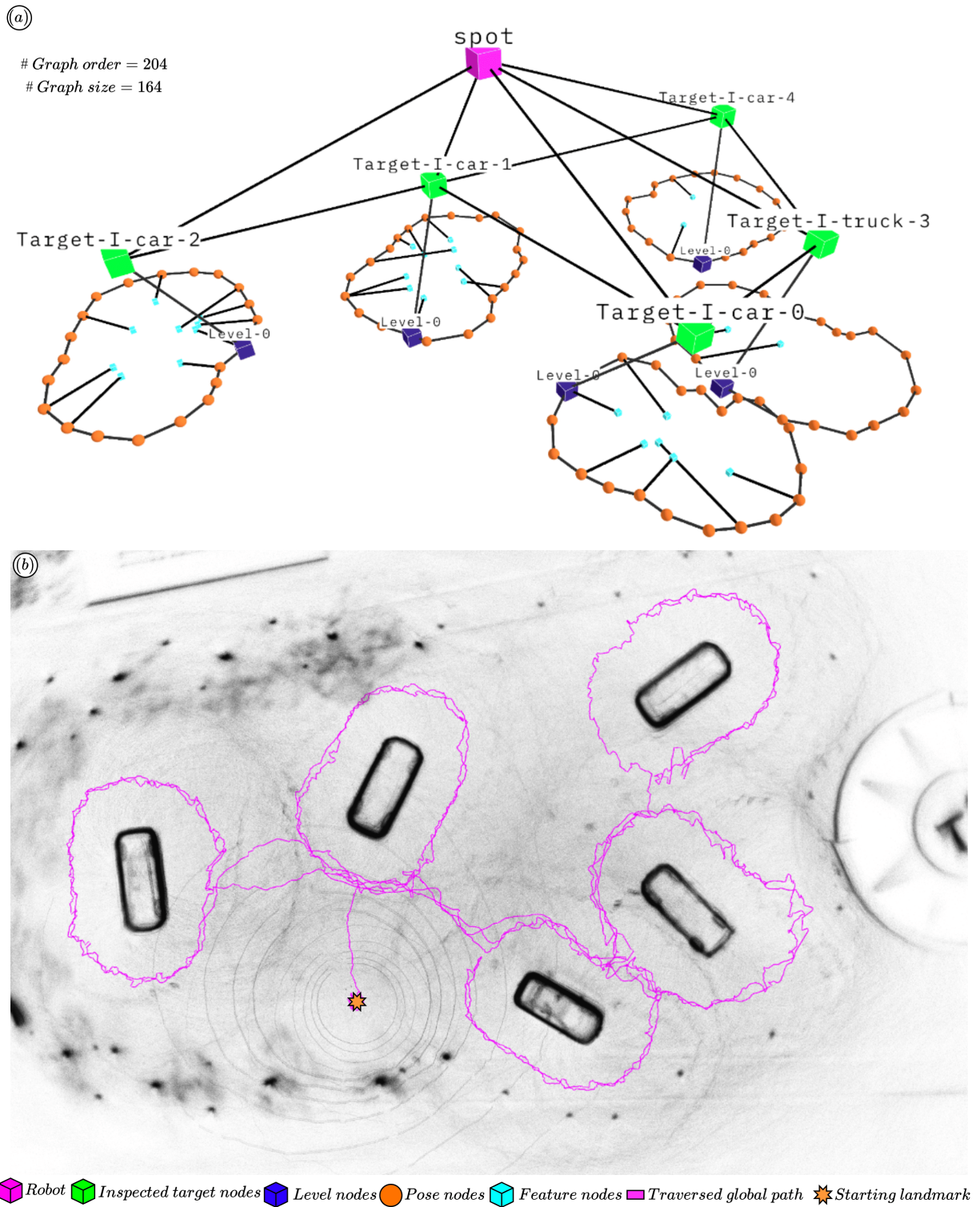


Fig. 27. A visualization of the results obtained for the five vehicle inspection scenario comprising of (a) the 3D LSG constructed during inspection alongside (b) the top-down perspective of the point-cloud map of the outdoor environment highlighting the inspected vehicles with the global traversed path.

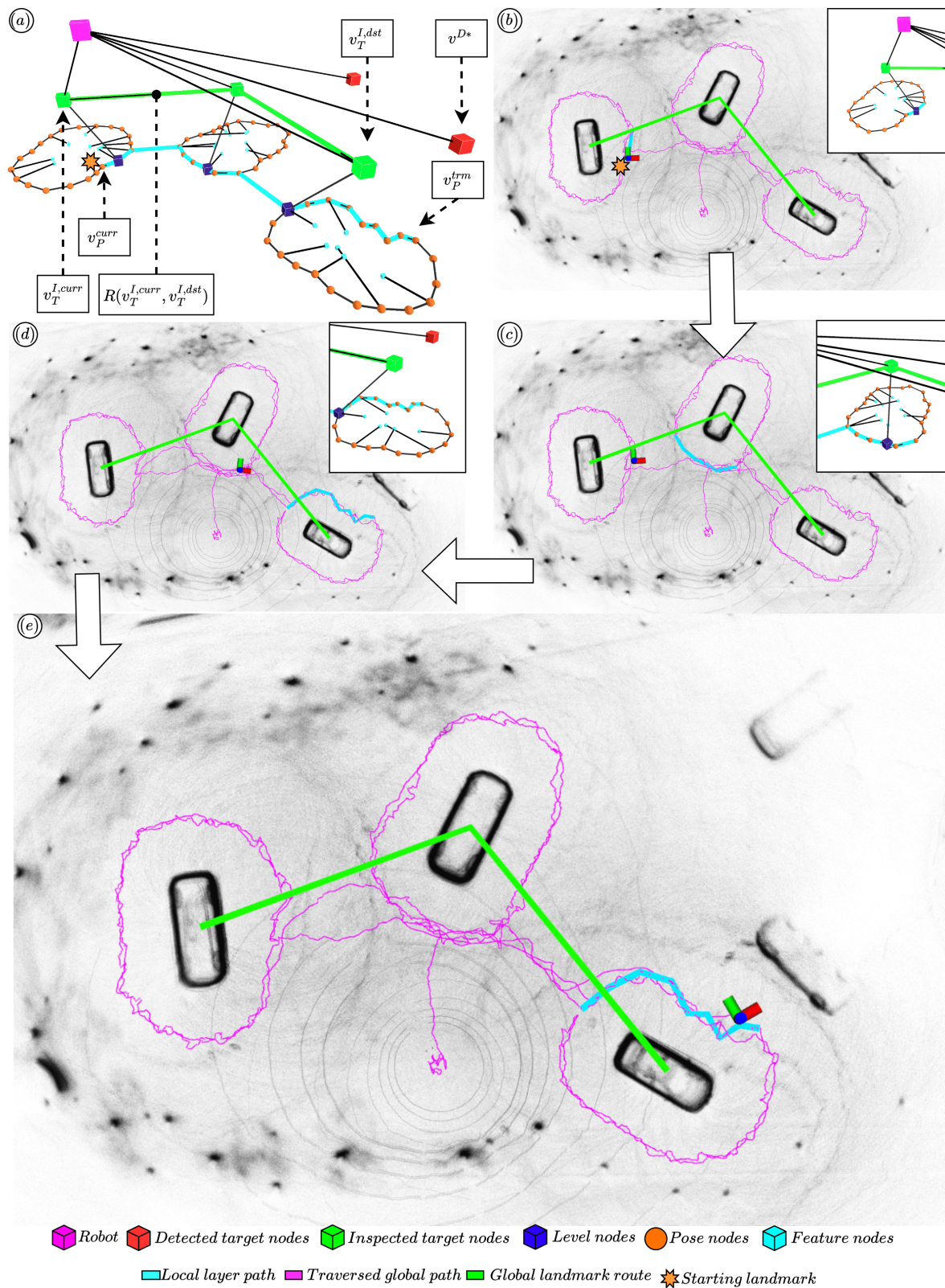


Fig. 28. A collage capturing the hierarchical planning process in response to a FLIE query to inspect a candidate semantic target v^{D*} . (a) highlights the global landmark route (shown in green) planned across the *Target* layer node alongside the local layer path (shown in cyan) planned across *Level* and *Pose* layers. (b) presents the first sequence of tracking the generated local layer path to move towards the nearest v_P of $v_T^{I,curr}$ in order to reach the next landmark node in sequence. The corresponding path planned across the 3D LSG is shown inset on the *top-right* corner. (c) captures the second segment of tracking the generated local layer path in order to reach the last landmark node $v_T^{I,dst}$ in the global sequence with the corresponding path across LSG shown inset on the *top-right* corner. (d) presents the last local segment planned to reach the evaluated v_P^{trm} to begin inspection of v_T^{D*} . Finally, (e) showcases the robot arriving at the v_P^{trm} and subsequently would start inspection of v_T^{D*} .

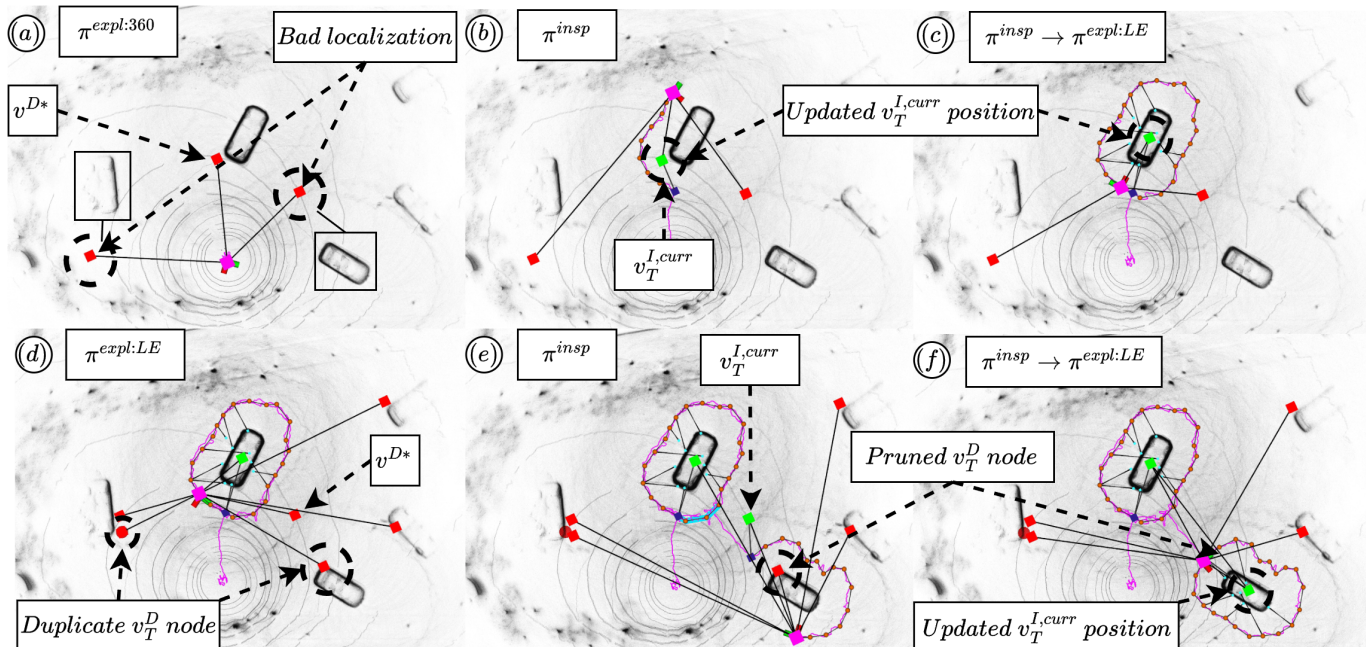


Fig. 29. A visual collage highlighting different instances during the inspection mission for a five vehicle scenario where the *Target* layer graph is pruned of low quality and duplicate observations of semantic targets. (a) presents the constituent nodes within \mathcal{G}_T , highlighting an instance after the initial exploration where the estimated location of two semantic targets diverged from its actual position, (b) continues the timeline of the mission showcasing the candidate semantic target being inspected. Note the off-centered localization of the inspected target node. (c) presents the instant FLIE planner switches to local exploration planning after terminating inspection. Additionally, the location of the inspected semantic target is updated based on the centroid of the constructed $\mathbb{P}^{v_T^I}$ representation. (d) visualizes \mathcal{G}_T during local exploration where duplicate semantic targets are observed and registered. (e)-(f) demonstrate an event where the polygon-based validation helps prune the *Target* layer graph, where in (e) the disparity between the estimated location of the candidate semantic target during the initial and latest observations is highlighted, (f) presents the event after \mathcal{G}_T update wherein the duplicate target node is removed after the containment check.

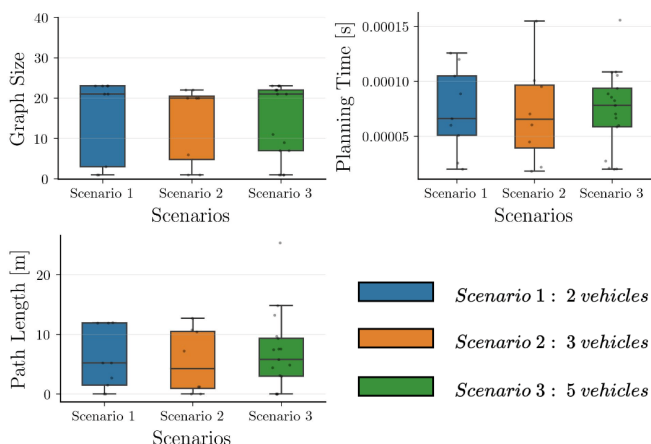


Fig. 30. A quantitative analysis of hierarchical planning performance during the experimentally evaluated inspection scenarios.

is highlighted in the evolution of Graph size plot (*top-left*) throughout the runs. This specifically demonstrates that the nested structure of LSG restricts the exposure of the graph-based path planner as it processes the graph to generate a traversable route. On the *top-right*, the time taken to generate a path is presented for each event a local graph is exposed to the path-planner. During the experimental runs, the median time for planning is capped under approximately 0.1 ms with maximum recorded value of approximately 0.16 ms .

Based on the behaviour of the planning performance seen for the simulated runs (refer Fig. 24), we expect a similar marginal increase in the planning time as the size of the environment increases. This is particularly due to the doubling in the graph size for the *Target* layer graph since the path-planner is agnostic of the class of registered edges, i.e. parent-child or child-child, in \mathcal{G}_T that should be used for planning a traversable path. A similar behavior is anticipated for the nested \mathcal{G}_L graphs as the number of inspection levels increases because of the existence of the dual class of edges within the *Level* layer graph as well. The recursive evaluation of the nested local layers is reflected in the recorded length of the planned path (seen in *bottom-left*), where the median tracked distance corresponds to the encoded edge weights of \mathcal{G}_P graphs.

During the evaluation of various scenarios in this work, particularly regarding the designed utility heuristic (refer to (2)), we observed that the factor S_p , which accounts for the proximity of the robot to the semantic target, plays a dominant role in decision-making when all three heuristics are weighted approximately similar. This resulted in a greedy approach where the nearest semantic target is always inspected.

Conversely, when the weight for the node centrality factor S_n —which considers the influence of neighbouring semantic targets—is significantly higher than S_p , the behaviour shifted to prioritize clusters of semantic targets over isolated, nearby ones. In extreme cases, if S_p is sufficiently high, the system would prioritize a distant cluster over a single, closer target.

This highlights a limitation: under real-world conditions with limited operational time and energy, such decisions are sub-optimal since the robot may run out of energy en-route to the distant semantic target. Comparatively, the model of $A(v^D)$ with the current low weight of S_r did not primarily influence the inspection decision as much as S_p and S_n contributed. However, this is only a matter of fine-tuning the values to reflect expected behaviour from the autonomy stack.

As a result, in order to move from the current static definition of the weights, we motivate as part of future work, the consideration of adaptive definition of the weights which influences the behaviour with respect to the remaining lifetime of the robot and the mission.

C. Feasibility Analysis of Planning Performance

To validate the benefits of constructing and maintaining an actionable hierarchical scene representation during inspection, we analyse the feasibility of planning over hierarchical graphs compared to conventional volumetric-based approaches during inspection. Specifically, we demonstrate the ease of executing a path-planning query over an hierarchical representation built by the inspection autonomy against traditional methods that build and plan over volumetric maps during inspection. To the best of the author’s knowledge, the proposed architecture is the first of its kind in integrating hierarchical scene graphs construction and exploitation with an inspection autonomy.

While there exists state-of-art methodologies that do graph-based planning over volumetric representation, they are either not available open-source [19] or do not support only planning query mode off-the-shelf [45]. Hence a one-to-one comparison is not possible. To that extent, for a given planning query during inspection, we compare the performance of the implemented hierarchical planner with an open-source grid-based path planner D_+^* [46] which operates over occupancy map representation such as Octomap [47]. For evaluation, we consider default parameters as available in the repository such as voxel size of 0.7 and risk value of 2. We run the octomap server during the autonomous inspection mission thereby building a volumetric model suitable for DSP to address the planning queries. We run the inspection mission and build the volumetric map for each individual scenarios. For the evaluation, we record the planning performance results for three scenarios with increasing size of total vehicles for inspection. In scenario one, we consider the case of five vehicle inspection while for scenario two, we demonstrate a ten car inspection. Finally, we pursue a twenty vehicle inspection scenario in scenario three.

Figure. 31 presents the comparative analysis of feasibility based on planning over hierarchical representations compared against conventional inspection methodologies that build and plan over volumetric representation. Figures. 31(a)-(c), present a runtime instance of the response of planning over volumetric (shown in *red*) compared against the path planned over hierarchical scene representation (shown in *green*) in terms of the global route planned to reach a queried semantic for increasing scale of the operating environment. Averaging the path length recorded over all three scenarios (refer Fig. 31(d)(*top*)), the

path planned over hierarchical representation is 7.9% shorter than the path planned over Octomap. This off-nominal behaviour can primarily be attributed to combination of large size of preset low voxel resolution of the map and the high risk value which altogether influences optimal collision-free path generation. However, increasing the resolution of the voxelized map directly impacts the computational overhead in terms of both memory occupied as well the time spent to plan a path, a characteristic noted by the authors in [46]. When compared with respect to the planning time (refer Fig. 31(d)(*bottom*)), the time spent planning over hierarchical representation presents an expected behaviour by exhibiting approximately 4 order of magnitude faster response to plan a path when compared against the response of planning over volumetric representation. Furthermore, there is a marginal increase in the time spent planning as the scale of the environment increases. This is in contrast to the behaviour seen for the time required to plan over a volumetric representation. While volumetric representations for path-planning is prominently beneficial in terms of enabling safe and collision-free navigation, it is more suitable for small-scale environments in terms of real-time implementation. As the environment size increases, hierarchical scene representation offer a rich and multi-resolution information which in addition, supports efficient manipulation of the data structure for addressing planning queries. The high-level route generated can then be later combined with volumetric representation to define a high-resolution collision-free and safe local paths.

D. Limitations

While the proposed architecture is extensively validated to address the task of inspection in unknown environments, it comes with a few limitations. During hierarchical planning, processing of the layer graphs for planning a feasible path is achieved by using a standard Dijkstra’s algorithm. Since Dijkstra’s path planner is agnostic to the type of edges that exist within an abstract scene graph, the naive consideration of both parent-child and child-child intra-layer edges contributes towards doubling the *Target* layer graph size with respect to the number of inspected targets. As a result, the time taken to process the graph increases. A potential solution to address this drawback is to implement a version of a graph-based path-planner that is aware of the abstract relations and able to parse necessary subset of intra-layer connections to address a given planning query.

Another smaller but relevant issue is the consideration of an overall static semantic target conditions during inspection and scene graph construction. While this assumptions holds if we consider an abandoned urban environment or the inspection of grounded targets such as buildings, it is especially highlighted when considering registration of dynamic targets-of-interest, such as moving cars, during exploration within the *Target* layer graph. Since this work does not account for spatio-temporal change in the scene during construction, subsequent inspection planning may terminate prematurely. Potential solutions to address this is beyond the current scope and is instead motivated to be part of future works.

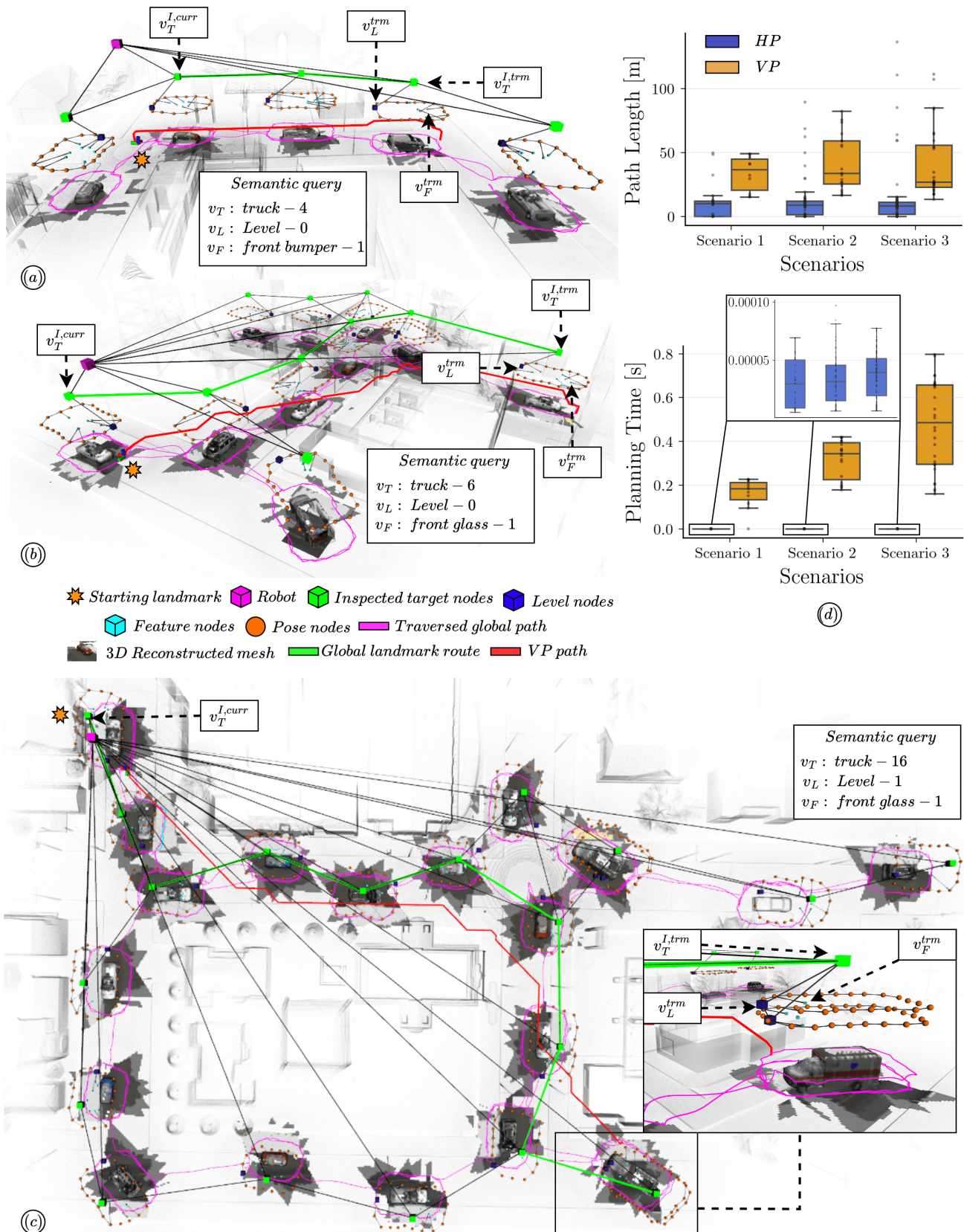


Fig. 31. A feasibility analysis for planning over hierarchical representation compared against a volumetric planner when considering environment scaling. The study is carried out for three scenarios, (a) scenario one, a five vehicle inspection, (b) scenario two, a ten vehicle inspection and finally (c) scenario three, a twenty vehicle inspection. (d) presents a boxplot visualization capturing the performance of both implemented approaches in terms of the overall planned path length and the time required to respond to each planning query recorded across all three scenarios.

VIII. FUTURE WORKS

Since the introduction of 3D scene graphs, the field of robotics has widely leveraged it to address a range of problems. In this work, we demonstrated the benefits of using a 3D scene graph for enhancing inspection planning in unknown environments. While the presented architecture holds the ingredients for a diverse collection of works that can be built upon existing framework, we summarize two main potential extensions that can be realized based off of the current achievement below:

(a) *Multi-modal task and mission planning*: The application potential for multi-modal task and mission planning is substantial, particularly when addressing multiple objectives within a single mission, such as exploration, inspection, search and rescue, or firefighting operations. The 3D LSG’s capability to interpret and respond to semantic queries offers a promising enhancement to mission planning. This system could be expanded to assign task-relevant platform modalities automatically based on the query type, increasing both efficiency and response accuracy.

The integration of Large Language Models (LLMs) enabled autonomy [48], [49] presents an exciting avenue to further enhance these capabilities. By leveraging LLMs, semantic queries can be translated into a sequence of smaller, executable tasks, allowing the system to break down complex objectives into manageable actions. This capability could streamline operations, thus enhancing the overall effectiveness of mission-critical deployments.

For instance, consider a semantic query like: “*Respond to fire-1 in Level-1 of house-2.*” The 3D LSG would process this input and through integration with an LLM, deploy a firefighting-capable platform to the designated area. Another example could involve a query such as: “*Start exploration after entering open-window-1 in Level-3 of building-1.*” Here, LSG alongwith an LLM, could influence selection of an appropriate platform capable of accessing the specified location, extract a traversible route from the 3D LSG and begin its mission accordingly.

(b) *Multi-agent autonomy*: The concatenation capability of various abstract layers within 3D LSG offer an application aimed towards multi-agent systems. Specifically, when considering two different platforms for exploration and inspection, the *Target* layer graph populated during exploration can be shared with another agent which subsequently populates the deeper local layers during inspection. This enables simultaneous operation of both agents while also potentially observing and characterizing more of the scene within the limited mission duration.

IX. CONCLUSIONS

We have introduced *xFLIE* architecture, comprising of a multi-modal planning autonomy *FLIE*, fully integrated with 3D LSGs, a real-time actionable hierarchical scene graph constructor, to address the task of inspection of apriori unknown targets of interest in unknown environments. Through extensive large-scale evaluations in simulated outdoor urban environments and corresponding field experiments utilizing a

quadruped robot, we demonstrate the performance of *xFLIE* in constructing, maintaining and exploiting an intuitive scene representation for autonomous inspection. Furthermore, we highlight the advantages of the latent nature of nested hierarchy within LSG for hierarchical path-planning. Moreover, we showcase online semantic path-planning capability from operator-defined semantic queries by leveraging the built LSG for addressing focused inspection tasks. Finally, we highlight the advantages of planning performance of utilizing hierarchical scene representations as an alternative to conventional volumetric representation for waypoint navigation in large-scale environments.

ACKNOWLEDGMENTS

The authors would like to acknowledge Elias Small and Jude Marroush for contributing in field evaluations.

The corresponding code for the work is available here: <https://github.com/LTU-RAI/xFLIE-key>.

REFERENCES

- [1] H. Li, G. Zhu, L. Zhang, Y. Jiang, Y. Dang, H. Hou, P. Shen, X. Zhao, S. A. A. Shah, and M. Bennamoun, “Scene graph generation: A comprehensive survey,” *Neurocomputing*, vol. 566, p. 127052, 2024.
- [2] U.-H. Kim, J.-M. Park, T.-J. Song, and J.-H. Kim, “3-d scene graph: A sparse and semantic representation of physical environments for intelligent agents,” *IEEE transactions on cybernetics*, vol. 50, no. 12, pp. 4921–4933, 2019.
- [3] I. Armeni, Z.-Y. He, J. Gwak, A. R. Zamir, M. Fischer, J. Malik, and S. Savarese, “3d scene graph: A structure for unified semantics, 3d space, and camera,” in *Proceedings of the IEEE/CVF international conference on computer vision*, pp. 5664–5673, 2019.
- [4] N. Hughes, Y. Chang, and L. Carlone, “Hydra: A real-time spatial perception system for 3d scene graph construction and optimization,” *Robotics: Science and Systems XVIII*, 2022.
- [5] Z. Jiao, Y. Niu, Z. Zhang, S.-C. Zhu, Y. Zhu, and H. Liu, “Sequential manipulation planning on scene graph,” in *2022 IEEE/RSJ International Conference on Intelligent Robots and Systems (IROS)*, pp. 8203–8210, IEEE, 2022.
- [6] Y. Zhu, J. Tremblay, S. Birchfield, and Y. Zhu, “Hierarchical planning for long-horizon manipulation with geometric and symbolic scene graphs,” in *2021 IEEE International Conference on Robotics and Automation (ICRA)*, pp. 6541–6548, IEEE, 2021.
- [7] R. Miao, Q. Jia, and F. Sun, “Long-term robot manipulation task planning with scene graph and semantic knowledge,” *Robotic Intelligence and Automation*, vol. 43, no. 1, pp. 12–22, 2023.
- [8] C. Agia, K. M. Jatavallabhula, M. Khodeir, O. Miksik, V. Vineet, M. Mukadam, L. Paull, and F. Shkurti, “Taskography: Evaluating robot task planning over large 3d scene graphs,” in *Conference on Robot Learning*, pp. 46–58, PMLR, 2022.
- [9] S. Amiri, K. Chandan, and S. Zhang, “Reasoning with scene graphs for robot planning under partial observability,” *IEEE Robotics and Automation Letters*, vol. 7, no. 2, pp. 5560–5567, 2022.
- [10] A. Rosinol, A. Violette, M. Abate, N. Hughes, Y. Chang, J. Shi, A. Gupta, and L. Carlone, “Kimeria: From slam to spatial perception with 3d dynamic scene graphs,” *The International Journal of Robotics Research*, vol. 40, no. 12-14, pp. 1510–1546, 2021.
- [11] S. Looper, J. Rodriguez-Puigvert, R. Siegwart, C. Cadena, and L. Schmid, “3d vsg: Long-term semantic scene change prediction through 3d variable scene graphs,” in *2023 IEEE International Conference on Robotics and Automation (ICRA)*, pp. 8179–8186, IEEE, 2023.
- [12] Z. Ravichandran, L. Peng, N. Hughes, J. D. Griffith, and L. Carlone, “Hierarchical representations and explicit memory: Learning effective navigation policies on 3d scene graphs using graph neural networks,” in *2022 International Conference on Robotics and Automation (ICRA)*, pp. 9272–9279, IEEE, 2022.
- [13] H. Bavle, J. L. Sanchez-Lopez, M. Shaheer, J. Civera, and H. Voos, “Situational graphs for robot navigation in structured indoor environments,” *IEEE Robotics and Automation Letters*, vol. 7, no. 4, pp. 9107–9114, 2022.

- [14] A. Werby, C. Huang, M. Büchner, A. Valada, and W. Burgard, “Hierarchical open-vocabulary 3d scene graphs for language-grounded robot navigation,” in *First Workshop on Vision-Language Models for Navigation and Manipulation at ICRA 2024*, 2024.
- [15] E. Greve, M. Büchner, N. Vödisch, W. Burgard, and A. Valada, “Collaborative dynamic 3d scene graphs for automated driving,” in *2024 IEEE International Conference on Robotics and Automation (ICRA)*, pp. 11118–11124, IEEE, 2024.
- [16] Z. Dai, A. Asgharivaskasi, T. Duong, S. Lin, M.-E. Tzes, G. Pappas, and N. Atanasov, “Optimal scene graph planning with large language model guidance,” in *2024 IEEE International Conference on Robotics and Automation (ICRA)*, pp. 14062–14069, IEEE, 2024.
- [17] Y. Liu, L. Palmieri, S. Koch, I. Georgievski, and M. Aiello, “Delta: Decomposed efficient long-term robot task planning using large language models,” *arXiv preprint arXiv:2404.03275*, 2024.
- [18] L. Schmid, M. Pantic, R. Khanna, L. Ott, R. Siegwart, and J. Nieto, “An efficient sampling-based method for online informative path planning in unknown environments,” *IEEE Robotics and Automation Letters*, vol. 5, no. 2, pp. 1500–1507, 2020.
- [19] M. Dharmadhikari and K. Alexis, “Semantics-aware exploration and inspection path planning,” in *2023 IEEE International Conference on Robotics and Automation (ICRA)*, pp. 3360–3367, IEEE, 2023.
- [20] C. Feng, H. Li, F. Gao, B. Zhou, and S. Shen, “Predrecon: A prediction-boosted planning framework for fast and high-quality autonomous aerial reconstruction,” in *2023 IEEE International Conference on Robotics and Automation (ICRA)*, pp. 1207–1213, IEEE, 2023.
- [21] C. Galindo, A. Saffiotti, S. Coradeschi, P. Buschka, J.-A. Fernandez-Madrígal, and J. González, “Multi-hierarchical semantic maps for mobile robotics,” in *2005 IEEE/RSJ international conference on intelligent robots and systems*, pp. 2278–2283, IEEE, 2005.
- [22] H. Zender, O. M. Mozos, P. Jensfelt, G.-J. Kruijff, and W. Burgard, “Conceptual spatial representations for indoor mobile robots,” *Robotics and Autonomous Systems*, vol. 56, no. 6, pp. 493–502, 2008.
- [23] Z. Zhou, R. Weibel, K.-F. Richter, and H. Huang, “Hivg: A hierarchical indoor visibility-based graph for navigation guidance in multi-storey buildings,” *Computers, environment and urban systems*, vol. 93, p. 101751, 2022.
- [24] S. Song and S. Jo, “Surface-based exploration for autonomous 3d modeling,” in *2018 IEEE International Conference on Robotics and Automation (ICRA)*, pp. 4319–4326, IEEE, 2018.
- [25] A. Bircher, M. Kamel, K. Alexis, H. Oleynikova, and R. Siegwart, “Receding horizon path planning for 3d exploration and surface inspection,” *Autonomous Robots*, vol. 42, no. 2, pp. 291–306, 2018.
- [26] M. Naazare, F. G. Rosas, and D. Schulz, “Online next-best-view planner for 3d-exploration and inspection with a mobile manipulator robot,” *IEEE Robotics and Automation Letters*, vol. 7, no. 2, pp. 3779–3786, 2022.
- [27] V. K. Viswanathan, B. Lindqvist, S. G. Satpute, C. Kanellakis, and G. Nikolakopoulos, “Towards visual inspection of distributed and irregular structures: A unified autonomy approach,” *Journal of Intelligent & Robotic Systems*, vol. 109, no. 2, pp. 1–24, 2023.
- [28] R. P. De Figueiredo, J. le Fevre Sejersén, J. G. Hansen, M. Brandão, and E. Kayacan, “Real-time volumetric-semantic exploration and mapping: An uncertainty-aware approach,” in *2021 IEEE/RSJ International Conference on Intelligent Robots and Systems (IROS)*, pp. 9064–9070, IEEE, 2021.
- [29] M. F. Ginting, D. D. Fan, S.-K. Kim, M. J. Kochenderfer, and A.-a. Agha-mohammadi, “Semantic belief behavior graph: Enabling autonomous robot inspection in unknown environments,” *arXiv preprint arXiv:2401.17191*, 2024.
- [30] A. Millane, H. Oleynikova, E. Wirbel, R. Steiner, V. Ramasamy, D. Tingdahl, and R. Siegwart, “nvbox: Gpu-accelerated incremental signed distance field mapping,” 2024.
- [31] G. Jocher, A. Chaurasia, and J. Qiu, “Ultralytics yolov8,” 2023.
- [32] T.-Y. Lin, M. Maire, S. Belongie, J. Hays, P. Perona, D. Ramanan, P. Dollár, and C. L. Zitnick, “Microsoft coco: Common objects in context,” in *Computer Vision—ECCV 2014: 13th European Conference, Zurich, Switzerland, September 6–12, 2014, Proceedings, Part V 13*, pp. 740–755, Springer, 2014.
- [33] G. Russo, “car-seg dataset.” <https://universe.roboflow.com/gianmarco-russo-vt9xr/car-seg-un1pm>, nov 2023. visited on 2024-01-24.
- [34] H. Louhichi, T. Fournel, J. Lavest, and H. B. Aïssia, “Self-calibration of scheinpflug cameras: an easy protocol,” *Measurement Science and Technology*, vol. 18, no. 8, p. 2616, 2007.
- [35] P. Lindenberger, P.-E. Sarlin, and M. Pollefeys, “Lightglue: Local feature matching at light speed,” in *Proceedings of the IEEE/CVF International Conference on Computer Vision*, pp. 17627–17638, 2023.
- [36] D. G. Lowe, “Object recognition from local scale-invariant features,” in *Proceedings of the seventh IEEE international conference on computer vision*, vol. 2, pp. 1150–1157, Ieee, 1999.
- [37] A. Ray, C. Bradley, L. Carlone, and N. Roy, “Task and motion planning in hierarchical 3d scene graphs,” *arXiv preprint arXiv:2403.08094*, 2024.
- [38] E. W. Dijkstra, “A note on two problems in connexion with graphs,” *Numerische mathematik*, vol. 1, no. 1, pp. 269–271, 1959.
- [39] T. Shan, B. Englot, D. Meyers, W. Wang, C. Ratti, and R. Daniella, “Lio-sam: Tightly-coupled lidar inertial odometry via smoothing and mapping,” in *IEEE/RSJ International Conference on Intelligent Robots and Systems (IROS)*, pp. 5135–5142, IEEE, 2020.
- [40] B. Lindqvist, S. S. Mansouri, A.-a. Agha-mohammadi, and G. Nikolakopoulos, “Nonlinear mpc for collision avoidance and control of uavs with dynamic obstacles,” *IEEE robotics and automation letters*, vol. 5, no. 4, pp. 6001–6008, 2020.
- [41] N. Koenig and A. Howard, “Design and use paradigms for gazebo, an open-source multi-robot simulator,” in *2004 IEEE/RSJ international conference on intelligent robots and systems (IROS)(IEEE Cat. No. 04CH37566)*, vol. 3, pp. 2149–2154, Ieee, 2004.
- [42] F. Furrer, M. Burri, M. Achtelik, and R. Siegwart, *Robot Operating System (ROS): The Complete Reference (Volume 1)*, ch. RotorS—A Modular Gazebo MAV Simulator Framework, pp. 595–625. Cham: Springer International Publishing, 2016.
- [43] A. Hagberg, P. Swart, and D. S. Chult, “Exploring network structure, dynamics, and function using networkx,” tech. rep., Los Alamos National Lab.(LANL), Los Alamos, NM (United States), 2008.
- [44] R. B. Rusu and S. Cousins, “3D is here: Point Cloud Library (PCL),” in *IEEE International Conference on Robotics and Automation (ICRA)*, (Shanghai, China), May 9-13 2011.
- [45] T. Dang, M. Tranzatto, S. Khattak, F. Mascariich, K. Alexis, and M. Hutter, “Graph-based subterranean exploration path planning using aerial and legged robots,” *Journal of Field Robotics*, vol. 37, no. 8, pp. 1363–1388, 2020. Wiley Online Library.
- [46] S. Karlsson, A. Koval, C. Kanellakis, and G. Nikolakopoulos, “Dsp: A risk aware platform agnostic heterogeneous path planner,” *Expert systems with applications*, p. 119408, 2022.
- [47] K. M. Wurm, A. Hornung, M. Bennewitz, C. Stachniss, and W. Burgard, “Octomap: A probabilistic, flexible, and compact 3d map representation for robotic systems,” in *Proc. of the ICRA 2010 workshop on best practice in 3D perception and modeling for mobile manipulation*, vol. 2, p. 3, 2010.
- [48] R. Royce, M. Kaufmann, J. Beckett, S. Moon, K. Carpenter, K. Pak, A. Towler, R. Thakker, and S. Khattak, “Enabling novel mission operations and interactions with rosa: The robot operating system agent,” *arXiv preprint arXiv:2410.06472*, 2024.
- [49] Z. Ravichandran, V. Murali, M. Tzes, G. J. Pappas, and V. Kumar, “Spine: Online semantic planning for missions with incomplete natural language specifications in unstructured environments,” *arXiv preprint arXiv:2410.03035*, 2024.